ABSTRACT

Title of Document: TOWARDS INTEGRATED FLUORESCENCE SENSING

Marc Péralte Dandin, Master of Science in Electrical Engineering, 2007

Directed By: Assistant Professor, Pamela Abshire, Electrical and Computer Engineering

This thesis is an account of ongoing efforts in the Integrated Biomorphic Information Systems Laboratory and the Laboratory for MicroTechnologies towards the implementation of integrated microfabricated biosensing platforms with on-chip fluorescence detection capability. The first chapter is a published, exhaustive, and critical review of state-of-the-art microfluorometers, and it offers a set of performance metrics for evaluating sensors of different architectures. The second chapter consists of material from two journal papers, currently in preparation, in which the development of a polymeric optical filter material for UV fluorescence spectroscopy is presented and its integration with a CMOS active pixel sensor (APS) discussed. The third chapter, which is also an archival publication, presents initial efforts towards achieving high-sensitivity CMOS photodetectors for use in photon counting-based fluorescence assays.

TOWARDS INTEGRATED FLUORESCENCE SENSING

By

Marc Péralte Dandin

Thesis submitted to the Faculty of the Graduate School of the
University of Maryland, College Park, in partial fulfillment
of the requirements for the degree of
Master of Science
2007

Advisory Committee:
Assistant Professor Pamela Abshire, Chair
Associate Professor Elisabeth Smela
Professor Neil Goldsman

Dedication

I dedicate this work to Carmélite, Marvel, Yanick, Sanite, and Siah. I thank you for your unconditional support, for your love over the years, for being my first line of defense despite the distance between us, and for being such an inexhaustible source of inspiration in my most difficult of moments.

This work is also dedicated to Louise and Edouard, *in memoriam*, and to the loving memory of many others I have lost and whose names I need not write here. I thank you for your love, your words, your wisdom, and your courage. But above all, I thank you for having nurtured in me, through your actions, the hope that our world will inevitably be, someday, a better place. You will always remain in my thoughts.

Acknowledgements

First and foremost, I would like to express my infinite gratitude to Pamela Abshire and Elisabeth Smela for their unwavering support during each step of this journey. I thank you for your mentorship, patience, and friendship, and for having given me the opportunity to explore the topics discussed herein. I am also indebted to Jon Orloff and Isaak Mayergoyz for having inspired and convinced me to pursue a graduate career. I also extend many thanks Neil Goldsman for evaluating this thesis and to Reza Ghodssi for his help with the ECE bureaucracy. I am very thankful to the University of Maryland's Mechanical Engineering and Bioengineering departments for offering me a home to continue this work.

I also thank my colleagues, past and current, for their advice and mentorship. I would particularly like to acknowledge, from Elisabeth's group, Mario Urdaneta, Remi Dellile, Xuezheng Wang, Marc Christophersen, Samuel Moseley, Pey-Shuan Jian, Steve Fanning, Wen Hsieh, Menake Piyasena, and Sheetal Patil. From Pamela's group, I would like to thank Nicole Nelson, David Sander, and Somashekar Bangalore Prakash for our fruitful ongoing collaborations. I would also like to thank Honghao Ji for having paved the way for some of this work, and Yiming Zhai, Alfred Haas, Anshu Sarje, Eric Wong, and Peng Xu for many discussions.

Finally, I would also like to take this opportunity to thank many individuals whose diligence has indirectly, nonetheless greatly, contributed to making this document a reality. I am grateful to Larry Pierre, from CHS-Miami, for his friendship and

support, and to Frantz Verella for his ongoing support, and for having brought me to the University of Maryland in 1999 following my failure to secure admission to the UEH School of Medicine. Many thanks also go to Marie-France and Rony Guiteau for their love and support. I thank Tipan, Jean-Max Cadet, and Tenoch for their friendship and support. I am also very thankful to Cynthia Sorrell for having been such a good friend over the years. And last, but not least, I extend my thanks to Curtis and John, my friends of old, for having taught me the most valuable lesson of all: the game can still be won even if you have just one chip left.

Chapter 1: Introduction

1 Background and Problem Statement

Over the past two decades, fluorescence spectroscopy [1] has emerged as an important analytical technique that has enabled significant breakthroughs in fields ranging from analytical biochemistry to clinical microbiology. For example, methods such as fluorescence resonance energy transfer (FRET) and fluorescence *in situ* hybridization (FISH) have been used, respectively, to quantify enzyme kinetics [2] and to perform genomic-based identification and differentiation of micro-organisms [3]. Fluorescence sensing is now an established optical imaging technique, and the number of applications in which it is used is rapidly increasing.

Researchers are now attempting to harness the benefits of fluorescence-based methods in micro-(total analysis systems) (μTAS) in order to perform on-chip detection and imaging. Integrated fluorescence sensing, combined with existing μTAS technologies such as microfluidics [4], capillary electrophoresis [5], and dielectrophoresis, to name a few, are expected to lead to compact, untethered, and disposable devices capable of performing complex on-chip biochemical analyses.

There are, however, many difficulties in integrating fluorescence sensing. One challenge is the engineering of appropriate microscale hardware for the separation of fluorescence from excitation light. In macroscale spectrometers, optical filtering is achieved with the aid of dispersive and free-space optical elements over relatively long optical paths; at the microscale, on the other hand, optical path lengths are inherently reduced due to miniaturization. Therefore,

the integration of detectors, analysis chambers, and optical filters in close proximity degrades the signal to noise ratio. The other noteworthy challenge is the design of highly sensitive detectors. Integrated platforms typically make use of conventional photodetectors for the detection of fluorescence. The noise levels of these detectors often do not allow the transduction of weak, fast-decaying, fluorescent signals. This thesis investigates both issues and presents early efforts towards high-sensitivity fluorescence transduction in integrated platforms.

2 Thesis Outline

The first chapter of the thesis, consisting of a multi-authored journal publication [*][6], offers a concise introduction to fluorescence sensing and further motivates the research highlighted in the remaining chapters. Moreover, it provides an exhaustive review of the state-of-the-art of microscale fluorescence sensors. The processes used to fabricate the microsensors were found to strongly influence performance and dictate the integration strategy. Therefore, a thorough analysis of these fabrication methods is given and their impact on performance is assessed. In addition, the paper provides a set of performance metrics for evaluating widely disparate microscale fluorescence sensor architectures in order to further advance the field.

Chapter 2 discusses the integration of a custom polymeric filter with a solid state photodetector chip. The fabrication of the filter consisted of loading an optically clear (i.e. with little absorption in the visible range of the electromagnetic spectrum) polymer matrix with an ultraviolet light-absorbing compound (a *chromophore*). The resulting composite was deposited

[*] This paper was written in collaboration with Pamela Abshire and Elisabeth Smela who both extensively contributed in revising the manuscript. Pamela Abshire also contributed the section on plasmonic interference filters and aqueous filters and was responsible for refining the derivation of the coupling efficiency equations. Elisabeth Smela also helped in developing the algorithm for accurately determining the filter cut-off.

onto a CMOS chip[†] to obtain a mesoscale integrated sensor for ultraviolet fluorescence spectroscopy. The potential for integration of the filter in microscale systems was demonstrated by showing patternability of the composite material using ultraviolet photolithography and dry-phase etching. The responsivity spectrum of the mesoscale sensor was measured in order to determine the wavelengths that the sensor can accommodate when used in fluorescence assays. The material from this chapter was adapted from two journal papers currently in preparation.

Chapter 3, which is also multi-authored[‡] [7], is an account of the design and test results from single photon avalanche diodes (SPADs) fabricated in a commercially available standard CMOS process. SPADs offer much higher sensitivity when compared to conventional CMOS active pixel sensors, and they will pave the way for fluorescence assays based on photon-counting techniques to be ported to microscale platforms.

[†] This sensor was designed by Honghao Ji and subsequent versions were adapted by David Sander.
[‡] This sensor was also designed by Honghao Ji. Nicole Nelson contributed the protocol for the titration assay demonstrated in this conference paper. Valeri Saveliev and Irving Weinberg provided acquisition hardware. Pamela Abshire helped in developing the testing procedures and in revising the manuscript.

Chapter 2: Optical Filtering Technologies for Integrated Fluorescence Sensors[§]

Abstract

Numerous approaches have been taken to miniaturizing fluorescence sensing, which is a key capability for micro-total-analysis systems. This critical, comprehensive review focuses on the optical hardware required to attenuate excitation light while transmitting fluorescence. It summarizes, evaluates, and compares the various technologies, including filtering approaches such as interference filters and absorption filters and filterless approaches such as multicolor sensors and light-guiding elements. It presents the physical principles behind the different architectures, the state-of-the-art micro-fluorometers and how they were microfabricated, and their performance metrics. Promising technologies that have not yet been integrated are also described. This information will permit the identification of methods that meet particular design requirements, from both performance and integration perspectives, and the recognition of the remaining technological challenges. Finally, a set of performance metrics are proposed for evaluating and reporting spectral discrimination characteristics of integrated devices in order to promote side-by-side comparisons among diverse technologies and, ultimately, to facilitate optimized designs of micro-fluorometers for specific applications.

1 Introduction

Cost reduction is not the primary motivation behind efforts towards miniaturizing fluorescence sensing. Rather, it is increasing capability. Fluorescence spectroscopy will be a key component of future micro-total-analysis-systems (μTASs [8]) which will integrate the capabilities of entire

[§] [6] M. Dandin, P. Abshire, and E. Smela, "Optical filtering technologies for integrated fluorescence sensors," *Lab Chip*, vol. 7, pp. 955 - 977, 2007.

laboratories onto compact devices consisting of microchips and other microfabricated elements. Such devices are already capable of performing complex chemical and biological experiments. Since the introduction of the first prototypes, these miniature systems have been demonstrated for numerous applications, ranging from immunoassays [9, 10] to pathogen detection and classification [11] to on-chip nucleic acid analysis [8, 12, 13]. State-of-the art μTASs also already automate steps such as sample preparation, handling, separation, and mixing [8, 12, 14].

However, despite the large number of microfabricated devices that make use of fluorescence spectroscopy as the detection modality [10, 13, 15-43], with only a few exceptions these microsystems still need to be interfaced with external, typically macro-scale equipment. Only high brightness samples can be used with existing micro-scale fluorometers. Fluorescence spectroscopy is still not "μTAS-ready," in the sense of completely micro-scale modules, because of the numerous technological hurdles facing the development of high-sensitivity integrated fluorescence detection (although there has been some miniaturization to produce portable fluorescence sensors [44-46]). Two of these challenges are low-noise optical detectors [47, 48] and optical filtering.

This paper focuses on the second challenge: integrated[**] techniques for separating the fluorescence light from the excitation light. It covers demonstrated, as well as promising, optical filtering techniques that realize *at least partial separation on-chip*.

[**] By integration we mean either *heterogeneous* integration, which consists of the assembly of several modules to form a single device, or *monolithic* (sometimes called homogeneous) integration, where each component is micromachined (bulk or surface) on a single substrate.

We begin with a brief overview of fluorescence sensing to lay the groundwork for evaluating the various filtering approaches. Each of the main technologies is then introduced in turn: interference filtering, absorption filtering, spectrally selective detectors, and controlling the path of the excitation beam. Each subsection begins with an overview of the physics behind the approach. This is followed by a description of the fabrication methods, since they determine the level of integration that is possible and since the techniques used in fabrication impact performance. The inherent advantages and limitations of the approach are then discussed, and representative micro-scale devices of that type are described. In the penultimate section, the performance metrics that have been achieved to date using the various approaches are compared, and suggested directions for future improvements are given. Finally, we end with a discussion of the performance standards that should be used to evaluate micro-scale fluorescence sensors.

2 Review of Fluorescence Spectroscopy

Fluorescence spectroscopy is well established and is the most powerful technique of molecular biology. Fluorescence assays are based on the excitation of particular molecular groups called *fluorophores*, which can be intrinsic to the specimen under study, introduced into it, or chemically bound to it [49]. Fluorophores are organic dyes that absorb light in one range of wavelengths and re-emit the light, called the fluorescence, in a range of longer wavelengths. Fluorescence spectroscopy is used for a wide variety of measurements, from simply detecting the presence of a species in a solution to monitoring complex biological processes like enzyme kinetics [49]. Its use in biomedical studies dates back to the late 1960s, when Herzenberg et al. introduced the fluorescence-based cell sorter [50], which allowed the sorting of live cells from dead ones using fluorophores as optical markers [51]. The next decade brought the capability of

single molecule detection, when Hirschfeld and his colleagues imaged a single antibody labeled with 100 fluorophores in a fluorescence microscope [52]. In the early 1980s, the field saw significant progress when Keller et al. detected a biomolecule labeled with a *single fluorophore* [53]. Today, fluorescence spectroscopy is ubiquitous in biomedical and biochemical analysis. The absorption spectrum, illustrated for a generic fluorophore in Figure 1, has a peak at λ_{ex}, and the emission spectrum has a peak at λ_{em}; the distance between λ_{ex} and λ_{em} is called the *Stokes shift*. Stokes shifts can be as small as 10 nm (Amplex UltraRed) or as large as 150 nm (Fura-2), depending on the fluorophore[††]. Note that the emission and excitation spectra shown in the figure are mirror images of each other; this is true for the majority of fluorophores. If the fluorophore is excited at an off-peak wavelength λ_{off}, the resulting fluorescence spectrum will be unchanged but will have a lower amplitude than if it is excited at λ_{ex} [1]. The number of photons emitted is typically much smaller than the number absorbed, reflecting the existence of non-radiative pathways for the decay of the fluorophore from its excited state. The ratio of the emitted to absorbed photons is the *quantum yield* of the fluorophore.

Fluorescence can be detected visually, for example using a fluorescence microscope, or it can be converted to an electrical signal in a fluorescence spectrometer. Although spectrometers have greatly improved over the years, their basic operating principle has not changed. They comprise an excitation source, a wavelength filter, and a detector [1]. The wavelength filter is of critical importance because it discriminates between excitation and emission photons by significantly reducing the excitation light intensity that reaches the detector while allowing through as much

†† Amplex UltraRed and Fura-2 are trade names for commercially available synthetic fluorescent probes. The Stokes shift data were obtained from http://www.invitrogen.com. Stokes shifts of natural fluorophores can be found in [49] N. Vekshin, *Photonics of Biopolymers*. New York: Springer-Verlag, 2002..

of the weak fluorescence signal as possible. This is essential because the excitation light is typically orders of magnitude brighter than the fluorescence signal. In conventional systems, the light directed at the sample is typically monochromatic at λ_{ex} and either comes from a laser or, more typically, is selected by a grating from a broadband source. In microsystems, however, the light source is often a broadband (40 to 90 nm FWHM[‡‡]) light emitting diode (LED).

In fluorescence sensing, the primary choices for the wavelength filters are *dichroic filters*. An ideal dichroic filter completely reflects one or more ranges of wavelengths (*optical bands*) and transmits other wavelengths with a nearly zero coefficient of absorption (dashed line in Figure 1).

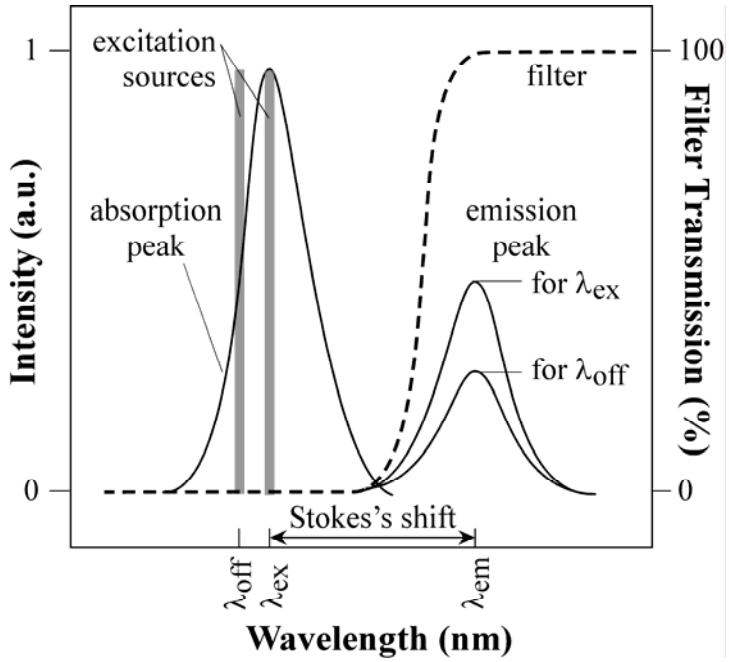

[‡‡] The "full width half max" (FHWM) of an LED is a measure of the spread around its peak wavelength. Here the term broadband is used in comparison to laser sources which have FWHM below 1 nm.

Figure 1. Typical peaks in the excitation (left) and emission (right) spectra. The wavelength filter (dashed line) must reject the excitation light and transmit the emitted fluorescent light. Excitation with off-peak (λ_{off}) wavelengths lowers the emission intensity.

Four parameters that characterize optical filters are *rejection levels* in the stopband (the wavelengths that are blocked), *transmission levels* in the passband (the wavelengths that are transmitted), and the location and sharpness of the transition between them, respectively known as the *absorption edge* and the *absorption edge width.* The first two metrics are based on the *absorbance*, which is defined as the base 10 logarithm of the ratio of the output light intensity to the incident light intensity: $A = \log(I_o / I_i)$. The absorbance includes losses due to absorption, reflection, and scattering. Intensity is defined as power per unit area, so we report rejection and transmission levels in decibels (dB), i.e. $10 \log(I_o / I_i) = 10A$. A rejection level is a value of $10A$ in the stopband, and a transmission level is a value of $10A$ in the passband; since $I_o / I_i < 1$, these numbers are negative.

Because practitioners in this field are from various scientific and engineering backgrounds, no consistent units have been used when reporting filter spectra. For example, spectra are reported in absorbance units *A*, linear units, or in cm^{-1}. For the devices reviewed in this paper, units were converted to dB, and those that were already reported in dB were assumed to be in the $10A$ format.

Ideally, one would want the filter to transmit 0% ($-\infty$ dB) of the excitation light and 100% (0 dB) of the fluorescence, and the absorption edge to be perfectly vertical and located to the right of λ_{ex} and to the left of the entire emission spectrum. In reality, these levels are unattainable, and the

stopband transitions to the passband over a range of wavelengths (the absorption edge width). The absorption edge width must be small enough to fit within the Stokes shift, as reported in [54] and illustrated in Figure 1. Otherwise, the fluorophore cannot be excited at the absorption peak, or all the emitted light cannot be collected, both of which decrease sensitivity.

3 Multiple Layer Interference Filtering

The earliest types of filter used at the micro-scale were interference filters, since these are traditionally utilized with fluorescence spectrometers at the macro-scale. These filters are essentially mirrors that reflect the unwanted light. When a broadband light beam impinges on alternating layers of materials with different indices of refraction, wavelengths that undergo constructive interference are transmitted, and those that add destructively are reflected [55]. The number of layers and their thicknesses can be designed to create a filter that transmits a desired spectral range. Such wavelength filters are also called *distributed Bragg reflectors* (DBRs).

Three physical facts govern their design [55]. The first is that the amplitude of the reflected light at any boundary between two media is given by $(1-\rho)/(1+\rho)$, where ρ is the ratio of the optical admittances at the boundary. The second is that there is a phase shift of 180^o when reflection occurs in a medium of lower refractive index, and zero phase shift otherwise. The third is that the reflected beam interferes destructively with the incident beam if the phase shift is 180^o and constructively if the phase shift is 0°.

Interference filters often have a quarter-wave structure in which each layer has a thickness of $n\lambda/4$, where n is the refractive index of the material and λ is the center wavelength of the

passband (set to the peak fluorescence wavelength) [55]. Such structures are known as *Bragg mirrors* or *Bragg reflectors*. Figure 2 shows the measured spectrum of a dichroic quarter-wave filter designed for use with the fluorophore FURA-2 (excitation: 365 nm, emission: 510 nm).

Band-pass filters can also be created. This is done by sandwiching a dielectric between two mirrors, which can be either Bragg mirrors or thin metal films, forming a solid Fabry-Perot cavity. For a guide to optimizing filter design, including how to determine the optimum number and thicknesses of the layers, how to deal with passband and stopband ripples (as are present in Figure 2), and how to minimize angle dependence, refer to [56].

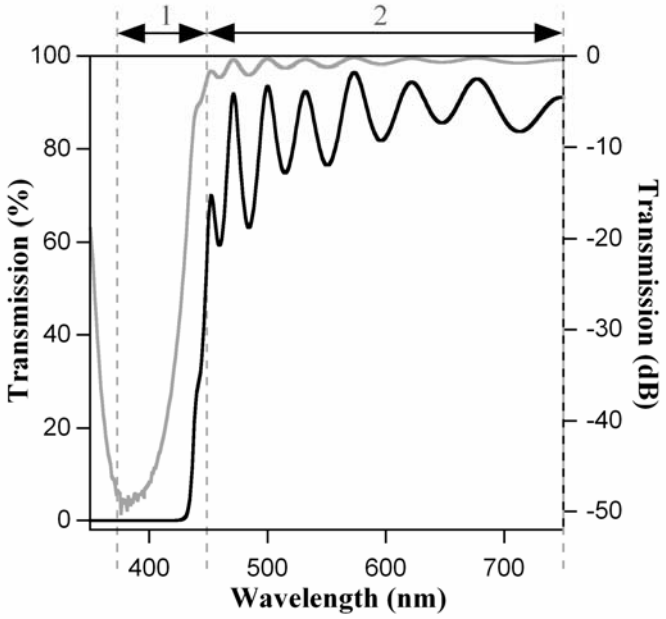

Figure 2. The spectrum, shown on both linear (black) and dB (gray) scales, of an interference filter with 39 alternating layers of PECVD-deposited silicon dioxide and silicon nitride, for a total thickness of 1.2 µm. Region 1 is the stopband of the filter and region 2 its passband.

3.1 Fabrication

Stacks of either dielectrics or semiconductors are used for quarter-wave filters that transmit in the visible. Their performance is generally comparable: although dielectrics do not attenuate optical wavelengths, and semiconductors do, the layers are so thin that absorption is negligible. A plethora of materials is available for the fabrication of interference filters, allowing one to achieve virtually any desired spectrum. Silicon dioxide, titanium dioxide, and silicon nitride are commonly used for visible light filters. Optical interference structures have also been made from compound semiconductors such as InGaAs, InP, and InGaN[55]. Metals, including Al and Au, are used in filters for infrared light.

The fabrication of interference filters is done with standard processes that can be performed at low temperature. Commonly used film deposition methods are plasma enhanced chemical vapor deposition (PECVD) for oxides and nitrides, sputtering or evaporation for metals, and molecular beam epitaxy (MBE) for compound semiconductors. Typically ~40 layers are required to obtain reasonable rejection.

3.2 Advantages and Limitations

One of the most important advantages of interference filters is that, since they can be fabricated using standard, low-temperature processes, they are compatible with integrated circuitry, and can be readily integrated into larger micro-scale systems. Another is the aforementioned freedom in the design of the absorption spectrum. Arbitrary spectral profiles can be obtained using different layer arrangements. This flexibility is the most important feature of multilayer interference filters.

However, they also suffer from some serious drawbacks. One important limitation of interference filters is that variations of a few nanometers in the thicknesses of the layers can cause large errors in the cutoff wavelength, up to +/- 50 nm. The thickness of each layer must be controlled to within 5% for a quarter-wave structure in order to preserve the targeted location of the absorption edge and achieve the desired transmission and rejection levels [55]. (Other structures such as half-wave stacks or Fabry-Pérot interferometers require even tighter tolerances [55].) If the fluorophore used in the assay has a small Stokes shift, with excitation and emission peaks close to the transition edge, exceeding the maximum allowable error is fatal to device performance. For example, the filter shown in Figure 2 was designed to have an absorption edge at 490 nm. Scanning electron micrographs of the stack revealed an average error of 12% (± 5 nm) in the nominal thickness of each layer. This produced a filter with an absorption edge at 430 nm. For assays with Alexa Fluor Hydrazide (488 nm excitation and ~30 nm Stokes shift), the excitation wavelength falls within the passband of this filter, rendering detection of fluorescence impossible. This highlights the need for stringent control during film deposition.

Moreover, the spectral response of these filters depends on the angle of incidence and the polarization of the incoming light, although design techniques can be used to minimize this [56]. The absorption edge of DBRs can shift by as much as 80 nm as the incidence angle is varied from 0 to 50° [54]. Another shortcoming, although not critical in most applications, is the presence of ripples in the transmission and stop bands, as illustrated in Figure 2. These ripples can be reduced by matching the optical admittance of the filter with that of the substrate.

Finally, it is not yet feasible to fabricate multiple filters of this type for different colors on one surface. Typically, the entire surface is coated and the filter is not patterned. This is because patterning is difficult if the layers are not etched by the same etchant. Given the effort required for deposition and patterning, interference filters remain the most challenging to integrate at the microscale.

3.3 Demonstrated Devices

This section highlights the systems microfabricated by Burns et al. [57], Adams et al. [58], Kim et al. [59], and Thrush et al. [60, 61]. Burns's device is one of the most highly cited in the literature because it beautifully illustrates not only integrated fluorescence, but also the lab-on-a-chip concept. Adams demonstrated the integration of filters and microfluidics with complementary metal oxide semiconductor (CMOS) imager chips, and Kim demonstrated the heterogeneous integration of detector, microfluidic channel, light source, and interference filter. Thrush accomplished the integration of the light source along with the filter and the photodetector.

3.3.1 Dielectric Quarter-Wave Stacks

Burns et al. fabricated a highly integrated μTAS for DNA analysis [5, 57, 62]. The fully automated system performed, on a single chip, several steps necessary for the sequencing of DNA. The device (Figure 3) consisted of the heterogeneous assembly of a nanoliter liquid injector, a sample positioning and mixing unit, a temperature-controlled reaction chamber, an electrophoretic separation system, air vents, and a fluorescence detector. The other components, including the light source and processing circuitry, were placed off-chip. A similar configuration

was described by the same group for a capillary electrophoresis device integrated with a fluorescence detector [62].

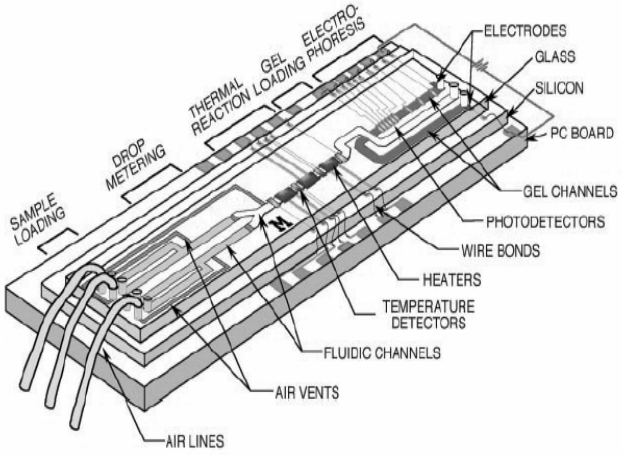

Figure 3. Schematic of a μTAS for DNA characterization that utilized a quarter-wave stack of SiO_2 and TiO_2 over the photodetectors. Reprinted with permission from [57]. Copyright 1998 AAAS.

The fluorescence sensor was a key component of this device, and it was used to detect the fluorescently-tagged DNA. The filter was a quarter-wave dielectric interference structure that transmitted the fluorophore emission wavelength (515 nm) and rejected the excitation wavelength (under 500 nm). Neither the number of layers nor the spectrum of the optical filter were reported.

Sensor fabrication started with the formation of a photodiode detector in a silicon substrate. Silicon dioxide was subsequently thermally grown over the photodiode to electrically isolate it from the other parts of the device, while still allowing light to pass through. A quarter-wave interference filter, consisting of alternating layers of silicon dioxide and titanium dioxide was then deposited by the thin film coating company ZC&R Coatings for Optics Inc. (Carson, CA).

Following this step, metal heaters were fabricated between two layers of vapor-deposited p-xylylene. These metal layers were used for temperature control and sensing. Platinum electrodes for electrophoretic separation were photolithographically defined on the surface of the upper p-xylylene layer. A glass chip containing etched microchannels was bonded to the surface to complete the assembly. Interfacing with off-chip control circuits was achieved via wirebonding of the pads to a printed circuit board.

This device demonstrated one of the benefits of μTAS: it performed DNA analysis with much smaller volumes than conventional fluorometers. In addition, the sensor could detect DNA at concentrations down to 10 ng/μL, which is impressive for a μTAS. Still, the authors acknowledged that one of the remaining technical challenges was to improve the sensitivity of the device. To address this issue, the authors later implemented more sensitive photodiodes that were able to detect a 100x lower concentration [62].

Adams et al. also made use of a quarter-wave dielectric filter, fabricating it on top of a CMOS imager [58]. This device is noteworthy because it integrated filters and fluidics with an on-chip camera, as opposed to discrete photodetectors. Such a configuration allows both quantitative and spatial analysis of fluorescence. This is an important feature for μTASs in which fluorescence is used not only as a detection mechanism but also as an imaging tool [63], such as is the case in microfabricated fluorescence-activated cell sorters (μFACS) [26].

The filter architecture was the same as that of Burns et al. The filter, which consisted of reactively sputtered silicon nitride and silicon dioxide, was deposited on top of the CMOS

imager. Following this step, a layer of PDMS that had been patterned with analysis chambers and channels was reversibly bonded onto the surface of the filter. An off-chip LED was used for excitation. The authors reported detection of fluorescein dye and blocking of over 99% of the excitation light.

This device also stands out because it integrated filters and microfluidics with CMOS. Post-CMOS fabrication processes are often challenging because of the tiny (mm^2) size of the microchips and because of more fundamental issues such as packaging, though these issues were not addressed by the authors.

Kim et al.[59] addressed both packaging and heterogeneous integration in their multi-module device, which included a detector, microfluidic channel, light source, and interference filter. The latter was a quarter-wave dielectric filter designed to attenuate 530 nm and to transmit 580 nm (the excitation and emission peaks, respectively, for tetramethylrhodamine (TAMRA)). While the spectrum showed a good transmission level of -1 dB at 580 nm, the decibel rejection level at 530 nm could not be determined from the given linear transmission spectrum.

The fabrication started by forming a p-i-n detector in a silicon wafer using photolithography and two cycles of ion implantation in order to obtain the desired doping levels. An interference filter comprising 32 layers of SiO_2 and TiO_2 with total thickness of 2.5 μm was then deposited over the surface. This photodetector substrate was then covered with a layer of PDMS. A microfluidic channel was defined in a second, soda-lime glass wafer, and on the back side of this wafer they fabricated an organic light emitting diode (OLED). The PDMS on the Si wafer was

bonded to the soda-lime wafer to seal the microchannels, making a sandwich structure comprising the OLED light source, microchannels, filter, and detector.

This architecture illustrates the integration of all necessary components for on-chip fluorescence detection. It is noteworthy because the fabrication is simple and integration tolerances, such as alignment error during assembly, are not stringent. The most challenging aspect of fabrication remains the control of layer thicknesses in the interference filter to achieve the desired spectral characteristics. The authors reported the detection of concentrations of TAMRA as low as 10 μM. The authors also demonstrated a similar architecture for the detection of Rhodamine 6G which achieved a detection limit of 1 μM [64].

3.3.2 Semiconductor Quarter-Wave Stacks

Thrush et al. developed a sensor (Figure 4) for use in deep-red to near-infrared fluorescence studies [60, 61, 65-69]. It consisted of a light source, a wavelength filter, and a photodetector, all micromachined on a single substrate. A second module was used for the microfluidic network containing the DNA sample, formed in PDMS. A commercially-available miniature lens glued over the sample chamber focused the fluorescence back onto the photodetectors.

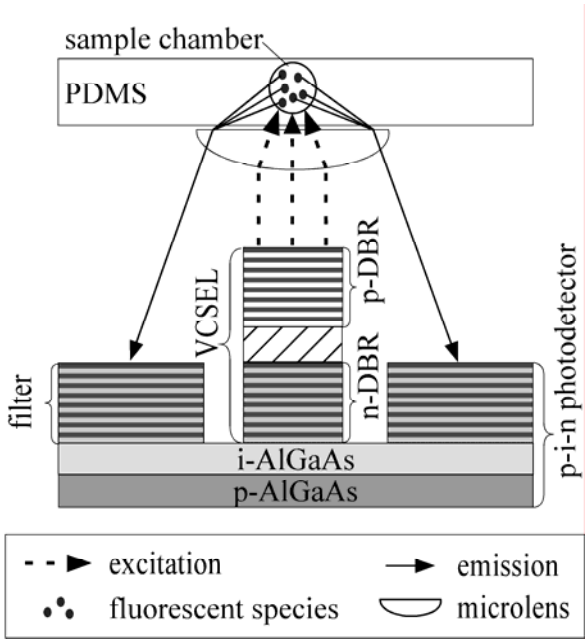

Figure 4. Integration of VCSEL light source, filter, and photodetectors (bottom) by Thrush et al. [60]. The microfluidics were housed in a separate module (top).

This design had several significant features, both from performance and fabrication standpoints. The authors used a vertical cavity surface emitting laser (VCSEL) as the on-chip light source, and they placed the detectors out of the direct optical path of the laser, thus combining interference and light-guiding spectral selection approaches. Because VCSELs emit exclusively in the direction normal to the surface, only the fluorescence focused by the lens (and a small amount of scattered excitation light) reached the detectors during the assay, allowing rejection levels of -40 dB [60].

DBRs served simultaneously as filters over the p-i-n photodetectors and as the n-type material in the photodetector structure. The i-AlGaAs layer and the AlGaAs DBRs were deposited by metallo-organic chemical vapor deposition (MOCVD) onto a p-AlGaAs substrate. The

deposition parameters were periodically varied to alter the stoichiometry of the compound. This produced a *single* layer of AlGaAs having 40 alternations in index of refraction forming the DBR, contrary to the previously described devices in which two dissimilar materials were used. There are several merits to producing a filter through index variations within a single material. The most important is that there is lower dispersion (the changes in index of refraction with frequency are similar for all layers), giving device performance that is easier to model and closer to the designed spectrum. Another is that it facilitates patterning. Finally, there is no mismatch in the coefficients of thermal expansion between the layers.

It is important to mention that this type of filtering differs from absorption filtering with semiconductors, discussed below. Although the DBR filter utilized a material with non-zero absorption, filtration was achieved exclusively by interference because the thickness of each "layer" was an order of magnitude smaller than the wavelengths used (both excitation and emission) in the assay. (For techniques on designing resonant cavities for semiconductor lasers and for information on MEMS-based semiconductor lasers refer to [70].)

A similar arrangement of components was used by Kamei et al. [71, 72]. However, there were separate modules for the detector and the filter, and an off-chip light source.

3.3.3 Porous Silicon Optical Filters

Another architecture for single-material interference filters is achieved by tailoring porous silicon. Porous silicon filters have been developed for other types of micro-spectrometers [73-76], but have not yet been demonstrated in fluorescence-based systems.

Pores ranging from nanometers to micrometers in diameter can be formed by bulk micromachining single crystal silicon through electrochemical etching [77-79]. The optical properties of porous silicon are controlled by varying the pore size and density as a function of depth into the wafer [80]. Refractive indices have been varied between 1.6 and 3.4 by modulating the porosity [77], which has allowed fabrication of filters over a wide range of the electromagnetic spectrum.

This technology could have significant impact on future devices, since the porosity can in principle be varied across the surface of the Si, allowing different spectral characteristics to be produced adjacent to each other simply by altering the etch parameters at a given location. This would enable multi-wavelength spectroscopy. Multi-wavelength capability would allow fluorophores of different colors to be detected on the same device, and thus enable more sophisticated assays that examine correlations between measurements. Multi-wavelength capability would also allow emissions from a single fluorophore to be stimulated or detected at different wavelengths, providing improved accuracy through the use of ratiometric measurements[§§]. Such design freedom and ease of fabrication would significantly extend the capabilities of micro-scale fluorescence sensing systems.

[§§] Ratiometric measurements rely on a differential response of the fluorophore at two wavelengths and can be done in one of two ways. In the first, two different frequencies are shone sequentially on the fluorophore, and the resulting emissions are measured. In the second, the emission at two wavelengths is monitored in response to a single excitation frequency. For a ratiometric dye, only one of these wavelengths is affected by the concentration of the analyte, so the ratio of intensities at the two wavelengths provides an estimate for the analyte concentration that is insensitive to changes in dye concentration, losses in the optical path, photobleaching, scattering, and background light.

As long as these filters can only be formed by bulk micromachining of single crystal material, monolithic integration with detectors and circuitry will not be possible. The technological hurdle to integrating such filters is producing porous silicon in thin films of amorphous or polycrystalline Si deposited onto a substrate. Promising attempts at producing porous silicon in films deposited on a substrate were made by Link et al.[81], however its use as an optical filter for fluorescence has not yet been demonstrated.

3.3.4 Plasmonic Interference Filters

Interference filters may also be constructed using structured metallic surfaces that discriminate between different wavelengths of surface plasmons[***], rather than of light directly. Plasmonic filters have been developed and characterized, but have not yet been demonstrated in fluorescence-based systems.

Many different plasmonic components have been demonstrated, including waveguides [82], mirrors [83, 84], interferometers [85], and Bragg gratings [85-88]. The Bragg gratings are typically realized in waveguide configurations using coupled metal-dielectric interfaces with periodic patterning imposed as gaps in a metal strip [87], changes in the thickness of a metal strip [86] or dielectric layer [89], changes in the width of a metal strip [87, 88], or changes in the dielectric constant of the dielectric layer [90, 91]. Although most existing plasmonic components have been developed and characterized at wavelengths relevant for telecommunications applications ($\lambda = 1550$ nm) [82, 86-91], a few components have been

[***] Surface plasmons are electromagnetic waves that propagate along the surface of a conductor, with exponentially decaying fields on either side of the interface. They arise from resonant interactions between a light wave and free electrons at the surface of the conductor and thus are confined spatially at the interface.

designed for operation at visible and near-IR wavelengths that are more appropriate for applications in fluorescence measurements [83, 92, 93].

This technology could have significant impact on future fluorescence sensing devices, since there is good potential for compact filters with different spectral characteristics to be implemented on the same substrate [94, 95]. This would enable multi-wavelength spectroscopy, as described above. Additionally, surface plasmons enhance fluorescence emission intensity [96-100]. This implies that it might be possible to create plasmonic devices that simultaneously enhance fluorescent emissions and filter excitation light [101, 102].

The primary drawback of plasmonic devices for spectral filtering is that the technology is not as mature as the other techniques discussed here. While the basic physical mechanisms have been known for several decades, the creation of such devices relies on nanostructured metal-dielectric interfaces, and fabrication of such structures has begun to be practical only within the last few years. Additionally, in order to use plasmonic filters for fluorescence, it must be possible to efficiently couple light into and out of surface plasmons. This is difficult because the momentum of surface plasmon waves is higher than the momentum of free space photons of the same frequency [94].

4 Absorption Filtering

An alternative to multiple-layer interference filters are single layers that have high absorption at the excitation wavelength but low absorption at the emission wavelength, known as *absorption*

filters. The absorption process is governed by the Beer-Lambert law: $I = I_0 e^{-\alpha x}$, where I is the intensity of the light exiting the filter, I_0 the intensity of the incident beam, α the *absorption coefficient,* a wavelength-dependent constant, and *x* the filter thickness. If the absorption spectrum of a material is known, the Beer-Lambert law can be used to find the absorbance *A* for a given thickness, and subsequently, the decibel representation of the transmission across the spectrum. Figure 5 shows absorption coefficient and transmission spectra for a few semiconductors and an organic chromophore that have been used for filtering.

There are two types of absorption filters, bandgap and organic, and both have been demonstrated at the micro-scale. Semiconductors make good absorption filters because of the energy gap between their valence and conduction bands [103, 104]: impinging photons with energies lower than the bandgap pass through, while photons with higher energies are strongly absorbed. Direct bandgap semiconductors (such as CdS, GaAs) have steeper drops in absorption coefficient (narrower absorption edge widths) in comparison with indirect bandgap semiconductors (such as Si).

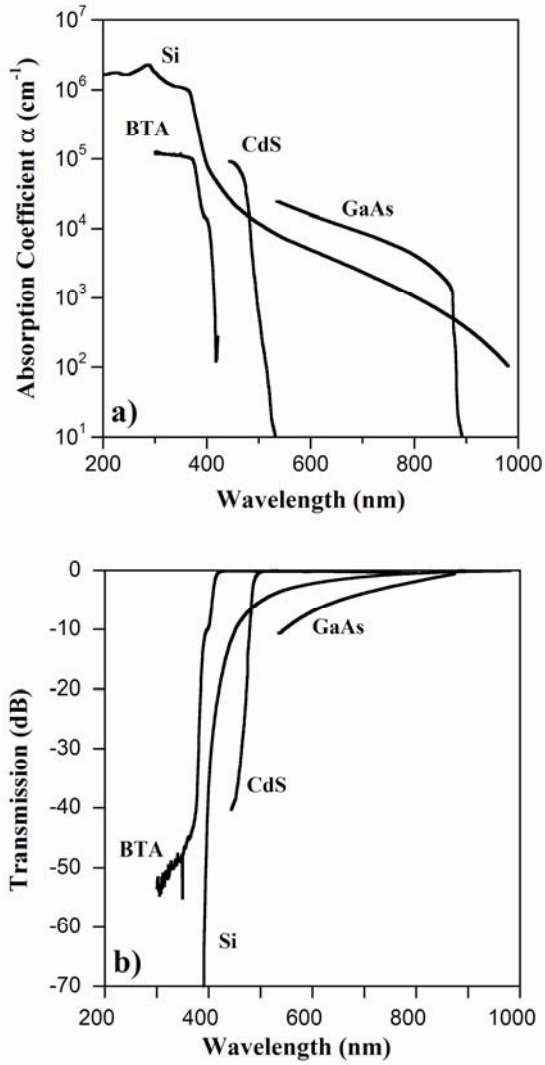

Figure 5. a) Absorption coefficient spectra of some common semiconductors and a chromophore, BTA, in an acrylic polymer host. Semiconductor data adapted from [103, 105, 106]. Data for 37 vol% BTA in acrylic are experimental results from our laboratory. b) Transmission spectra calculated from the absorption coefficient spectra.

Organic absorption filters are chromophore-based. *Chromophores* are molecular groups that absorb light with no subsequent re-emission. Polymer filters contain chromophores either as part of their molecular structure (intrinsic) or as guests (extrinsic) in the polymer host [107].

4.1 Fabrication

Essentially all semiconductor deposition methods can be employed to deposit thin films for absorption filtering. CVD, low pressure CVD (LPCVD), PECVD, pulsed laser deposition (PLD), and MBE are the most common [108]. For some materials, the absorption edge can be tailored by controlling the deposition conditions. For example, the bandgap of hydrogenated amorphous silicon has been varied from 1.2 eV to 3.3 eV by adjusting pressure and gas flow rates during PECVD [109].

The main advantage of polymer filters is that they can be deposited and patterned simply and at low cost by a wide variety of methods, usually at room-temperature, with minimal residual stress even in thick films. Polymers can be deposited by spin-coating or casting (for thicker layers) when the polymer is either a precursor that requires a curing step or a polymer dissolved in a solvent that evaporates. Curing methods vary depending on the polymer: some are cured by ultraviolet exposure, whereas others require a thermal cycle or the addition of a cross-linking agent.

4.2 Advantages and Limitations

Fabrication is more straightforward for absorption filters than for interference filters, since it requires only a single layer and no tight tolerances. Another advantage is that, unlike for multi-layer filters, the response of the filters is independent of the angle of incidence. On the other hand, a disadvantage of absorption filters is their limited tailorability compared with interference

filters; instead, the material must be chosen to be compatible with a specific fluorophore, which can entail complete changes in fabrication methods for different applications of the same device.

Semiconductors show a remarkable ability to absorb ultraviolet light. For example, high energy ultraviolet light (200 nm) is reduced by a factor of ~3 in only 10 nm of silicon. However, a major drawback is their lack of dichroism. As can be seen in Figure 5, the absorption coefficient for some materials is non-zero from the ultraviolet to the infrared regions of the electromagnetic spectrum. This means that 0 dB transmission of short Stokes shifted fluorescence emissions is impossible with most semiconductor filters. Though this is not an issue for high brightness applications, it is in assays with low fluorophore concentrations.

For polymeric filters based on absorption by a chromophore mixed into the polymer matrix, the spectrum can be modified through the choice of the chromophore, but the dye must be soluble in the host. Extrinsic chromophores loaded into an optically clear matrix can offer high rejection, as shown in Figure 5. Rejection can be increased without increasing film thickness by adding more chromophore to the host, until it saturates. Dandin et al. [110] demonstrated the loading of 2-(2'-hydroxy-5'-methylphenyl) benzotriazole, BTA, which is a photo-stable UV-absorbing chromophore, into several polymers. They were able to achieve -45 dB rejection of excitation wavelengths and -1.5 dB transmission of emission wavelengths in only 1 μm thick films. In addition, the chromophore exhibits dichroic behavior, so the absorption edge was steep. It should be mentioned that loading of photo-active organic compounds into polymers has previously been proven to be effective in other commercial applications, such as thin-film

polymer displays [111, 112], multi-wavelength photoresists [113], photostabilization of polymers for sunlight protection [107, 114], and cataract surgery [115].

4.3 Demonstrated Devices

Several devices in the literature have made use of single-layer absorption filters. The first that we review in this section, developed by Chediak et al. [54], integrated the light source, detector, and filter. These authors also presented a useful quantitative comparison of single layer semiconductor filters versus DBRs. The second, developed by Iordanov et al. [116], stands out because it integrated filters and microfluidics and, like Adams [58], used a CMOS imager.

Chabinyc et al. [117] demonstrated a device that used a polymeric filter, and similarly Kruger et al. [118] used a commercially-available gelatin filter. Hofman et al. used a millimeter-thick dye-doped PDMS film both as a microfluidic network and as a fluorescence filter [119]. These devices are not discussed further here because of the thicknesses of the polymer filter films; however, they do illustrate the technique of loading chromophores into optically clear polymers for fluorescence sensing applications.

4.3.1 Cadmium Sulfide Filters

Chediak et al. [54] demonstrated a micro-fluorometer based on the heterogeneous integration of CdS filters with InGaN LEDs (Figure 6). CdS was used because of its sharp absorption edge at 513 nm (20 nm wide): the device was used to detect blue-excited, green-emission fluorophores.

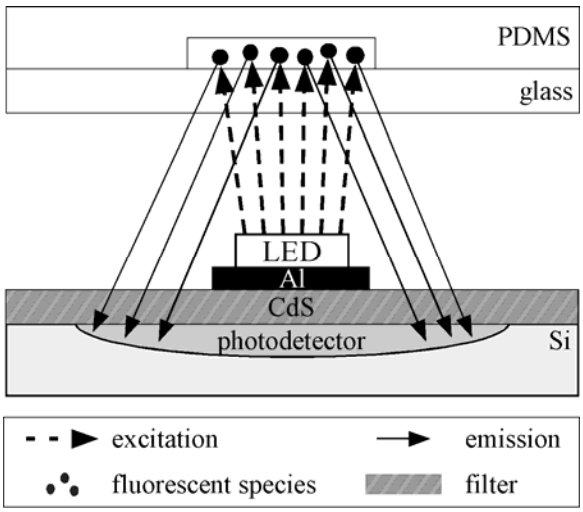

Figure 6. A microfluidic channel module assembled with a detector chip that has a CdS filter and Si photodetector onto which an LED has been mounted over an Al bond pad [54].

This device configuration was essentially the same as the one in Figure 4, but without a lens. It consisted of two modules. The sensing module included a silicon photodetector onto which the CdS filter was deposited by PLD. An InGaN LED (primarily blue emission) grown on sapphire was bonded to an aluminum bondpad that had been deposited and patterned over the filter to provide electrical connection. The aluminum served a critical secondary role as a reflector of the weaker green emission of the LED: these wavelengths lay in the transmission band of the filter and had to be blocked. A separate sample-containing module consisted of analysis chambers and a microfluidic network formed in PDMS. The PDMS was bonded to a glass substrate and positioned 2 mm above the LED.

The authors characterized a 2.4 μm CdS film. It had -60 dB rejection of the excitation light at 470 nm (i.e. 99.9999% of the light blocked, or 10^{-6} of the light transmitted) and -4 dB (40%) transmission of the fluorescent wavelength (513 nm). However, only a 1.2 μm film was used in

the prototype, and its rejection and transmission metrics were not provided. From Figure 5 and the Beer-Lambert law we estimate the transmission to be -30 dB at the excitation wavelength and -0.05 dB at the emission wavelength of the fluorophore. The device was able to detect a concentration of fluorescein as low as 0.12 μM. The authors likely used a thinner film in order to enhance transmission of the fluorescence and increase device sensitivity.

4.3.2 Poly-Si Filters

Iordanov et al. used a single layer of poly-crystalline silicon (polySi) to filter ultraviolet light but transmit light at 450 nm to a custom-made CMOS imaging array (Figure 6) [116]. They fabricated a microfluidic network over the sensor and used the device to perform enzymatic analyses, specifically monitoring NADH concentration. They used the imager for monitoring fluorescence on different areas of the chip.

After completion of the CMOS fabrication process, the polySi thin film filter was deposited using LPCVD over the passivation layer. Filtering characteristics were improved if the grains of the polySi were enlarged through a subsequent pulsed XeCl excimer-laser annealing step. A microfluidic network was built on top of the filter using the negative photoresist SU-8. Packaging and integration issues must have been challenging but were not explicitly addressed. The authors reported that the device detected fluorescence with 35 dB selectivity (ratio of the signal from the fluorescence to the signal from the excitation light). Unfortunately, they did not provide results characterizing the performance of the filter alone.

4.3.3 Polymer-Based Filters

Chabinyc et al. demonstrated a simple fluorescence sensing system that employed polycarbonate as a filter [117]. This system was not integrated, but rather used a multimode optical fiber inserted into a microchannel fabricated in PDMS to couple light into the microchannel. A commercial micro-scale avalanche array detector was embedded into the PDMS at the other end of the channel. The avalanche array detector was coated with 80 μm of polycarbonate.

The device was calibrated by filling the channel with known concentrations of the fluorophore in water. The sensor was able to reproducibly detect concentrations as low as 25 nM. No data were reported on the spectral characteristics of the polymer filter.

4.3.4 Aqueous Filters

Schueller et al. [120] and Chen et al. [121] demonstrated absorption filters using water-soluble dyes that were spatially patterned using an array of parallel microfluidic channels. These systems have the advantage of being able to reconfigure the filter during operation for different desired characteristics by filling the channels with fluids having different optical densities and different spectral characteristics. However, this technique has not yet been demonstrated in fluorescence-based systems.

5 Spectrally Selective Detectors

Thus far we have reviewed filtering approaches that prevent the excitation light from reaching the detector by either reflection (through interference) or absorption. A relatively new approach

is to collect both fluorescence and excitation components and discriminate between the two electronically. This is possible because semiconductor detectors are spectrally selective, as implied by the absorption coefficient curves shown in Figure 5. Multi-color sensors can be obtained by exploiting this spectral selectivity.

The physical principles are identical with those responsible for the operation of absorption filters – namely, that absorption is a function of both material composition and wavelength. Absorption of photons above a critical energy in a semiconductor creates electron-hole pairs that can be separated and collected. These carriers may be used to produce a current, charge, or voltage signal that is directly proportional to the intensity of the incident light. Three devices that use these principles are described in this section.

One method for realizing spectrally selective sensors is by using a variety of different semiconductors. Clearly, different semiconductor materials can exhibit distinctly different spectral responses as a result of the underlying differences in their electronic properties.

The second approach makes use of the fact that light of different wavelengths is absorbed at different depths in a semiconductor photosensor, giving spectral selectivity within a single material. Shorter wavelength photons are absorbed at the surface, longer wavelength photons deeper in the material, although both decrease exponentially by the Beer-Lambert law. Spectral components can be separated by collecting photo-generated carriers at different depths using, for example, three vertically-stacked p-n junctions as illustrated in Figure 7 [122]. The p-n junctions of such a pixel have different, broad spectral responses, or *selectivities*, similar to the responses

found in cones, the photosensitive cells of the retina. Even if each junction is sensitive to all of the incident wavelengths, it is differently sensitive to each, and so to identify the intensities of the 3 known wavelengths from the 3 broad spectral bands is a simple matter of solving a set of algebraic equations.

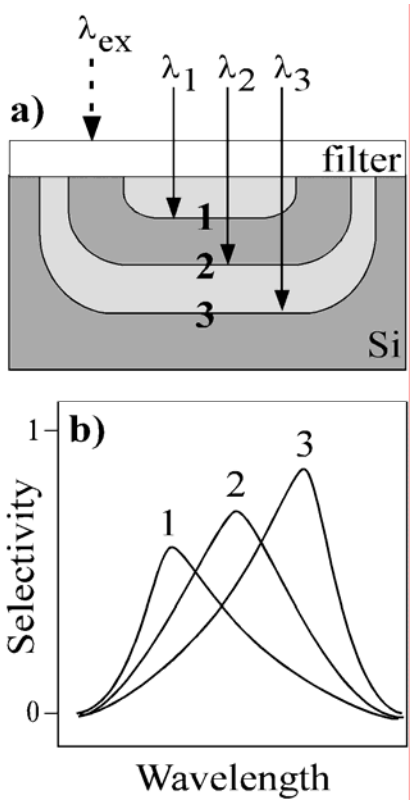

Figure 7. a) Multiple p-n junctions at different depths collect different spectral components of the fluorescence, λ_1, λ_2, and λ_3. The excitation light (λ_{ex}) is blocked by the filter. b) Spectral selectivities of each of the three coincident p-n junctions. Figure adapted from [123].

5.1 Fabrication

Layered semiconductor structures can be constructed using standard CMOS fabrication techniques, a significant benefit for integration. These architectures are not limited to silicon, though: the deposition processes discussed previously for other semiconductor materials can also be applied to the construction of spectrally selective detectors.

5.2 Advantages and Limitations

Multi-color sensors are of significant importance to micro-scale fluorescence-based systems. The architectures discussed so far targeted specific applications and are limited because they can only accommodate specific fluorophores. Multi-color sensors offer more versatility because they can detect several emission wavelengths.

Unfortunately, the spectral components collected by a multi-color sensor might not match the fluorescent wavelengths for a specific application, which could reduce the accuracy of the intensity estimation. This would occur because the spectral selectivity is determined primarily by the material properties, rather than by components in the system design such as readout circuits or physical layout. Therefore, it is necessary to tightly control film deposition parameters and it may be necessary to tweak the fabrication process. In most cases this is impractical or prohibitively expensive for CMOS technologies. For this reason, it may be advantageous to combine the fabrication of such sensors with the micro-machining of the optical filters.

5.3 Demonstrated Devices

Two macro-scale devices that demonstrate the use of spectrally selective detectors for fluorescence sensing can be found in the literature; this concept has not yet been used in an integrated device. The first, by Starikov et al. [124] used several MBE-grown diodes in order to obtain a wide range of spectral characteristics. This work is remarkable because it also made use of the detectors as light sources. The second device, developed by Maruyama et al. [125, 126], is important because it shows the use of a CMOS-fabricated photogate pixel to achieve fluorescence detection. Neither of these devices made use of an optical filter.

5.3.1 Heterojunction Detectors

Starikov et al. [124] demonstrated the use of spectrally selective photodetectors in detecting multi-wavelength fluorescence. The photodiodes were p-n heterojunctions of the wide bandgap semiconductors AlGaN and InGaN, which were fabricated by molecular beam epitaxy. Optical selectivity was achieved by varying the composition of the AlGaN/InGaN alloy to achieve different emission and photoresponse spectra in different devices. The diodes could be toggled on or off to serve either as photodetectors or light sources.

Multi-wavelength fluorescence detection was achieved by placing 8 diodes, with spectral characteristics ranging from the ultraviolet to red, in a circular pattern around an analysis chamber containing the analyte. The diodes were used for either excitation or collection of the fluorescence. Assays with several fluorophores (fluorescein, chlorophyll, pyrene, green fluorescence protein (GFP), and red fluorescence protein (RFP)) were conducted as a proof of concept. A detection limit of 2 nM of fluorescein was achieved.

5.3.2 Photogate CMOS Pixel

Maruyama et al. [125, 126] extended the concept of Figure 7 by using a photogate pixel for collection of fluorescence. Rather than stacking a series of junctions, the depth of the sensing region was controlled by the voltage applied to the photogate. A *photogate* is a single-element surface-channel charge-coupled device. Photo-generated charges are collected in a depletion area formed underneath the photogate, which in this case was formed using polySi over a p-n junction formed by a moderately doped p-type region (p-well) in a lightly doped n-type substrate.

By varying the gate voltage, these authors were able to vary the collection depth, and thus to modulate the spectral responsivity of the device. The pixel was fabricated using standard CMOS technology and was able to discriminate between blue and green wavelengths without the use of a filter. The sensor was used to detect a solution containing double-stranded DNA labeled with the fluorescent nucleic acid stain SYBR-Green, with an estimated detection limit of 10 μM.

6 Light-Guiding Elements

Thus far, we have reviewed on-chip filtering and detection techniques based on optical interference and light absorption. A completely different approach consists of exploiting ray optics to achieve separation of excitation and fluorescence, either with waveguides or with microfabricated free-space optical elements. The basic idea in both cases is to use geometry and optics to prevent the excitation light from falling on the detector. This is possible because the excitation light is collimated, and can therefore be guided, while the fluorescence is emitted in all

directions. Lenses, gratings, mirrors, and prisms have been miniaturized for this purpose. A wealth of information is available on the fabrication and integration of these elements for other types of micro-spectrometers [127, 128]. In this section, we review those devices that have used light-guiding elements to achieve at least some degree of on-chip filtering.

6.1 Fabrication

The fabrication methods used to produce miniature fluorescence sensors based on filterless techniques vary greatly because of the large variety of implementations. Thus, fabrication information is provided below, together with each of the demonstrated devices.

6.2 Advantages and Limitations

Filtration of excitation light without a thin film filter is attractive because it can be achieved using free-space optical elements simply by collimating the excitation and positioning the detector away from the optical path. The waveguiding schemes provide the same advantage, but can be limited by the performance of the waveguide. Non-idealities due to fabrication imperfections, such as waveguide sidewall roughness, or to misalignment in coupling the excitation light into the waveguide affect the extent to which the fluorescence is guided without loss and the extent to which the excitation light is excluded from the detector.

Another attractive feature, if not the most important, is the ability to combine this filtering approach with those previously discussed. We presented the Thrush and Chediak devices as architectures using thin-film filters, but positioning played an important role in preventing the excitation light from falling on the detector. Thrush (Figure 4) used the vertical emission of the

VCSEL to ensure that minimal excitation light reached the filter-protected detectors and a microlens to focus maximum fluorescence light onto the detectors. In later work, Thrush incorporated metal sidewalls on the detector to enhance optical isolation and rejection levels [67, 69]. Similarly, the Chediak architecture (Figure 6) used positioning to avoid saturating the fluorescence collected by the CdS-protected detector.

Unfortunately, measurements that describe the extent to which rejection has been achieved or to which fluorescence has been collected with miniaturized light-guiding technologies have not been reported: metrics analogous to absorption and transmission for filters have not been developed to characterize the performance of filterless devices. Rather, it has been more common to report the signal to noise ratio (SNR). This makes comparison among different device types difficult, since the SNR depends not only on fluorescence signal, but also on the photodetector characteristics, such as the dark current level or other sources of electronic noise.

6.3 Demonstrated Devices

The light-guiding approach has been popular, with quite a few devices reported in the literature [129-146]. The majority of these devices make use of orthogonal or angled positioning of the waveguides to obtain some degree of spectral separation. However, most of them still rely on off-chip filters or spectrometers to completely isolate the fluorescence from the background excitation light.

Another approach is to use micromachined free-space optical elements to achieve on-chip filtering. Two of these that demonstrate the free-space optical element approach are reviewed

here as representatives of the types of architectures that have been employed. The first, by Roulet et al.[136-138], integrated microlenses with microfluidic modules. The second, by Zeller et al. [134], demonstrated excitation and sensing with a single microfabricated grating.

6.3.1 Waveguides and Fiber Optics

The classical definition of the term waveguide is any structure that routes electromagnetic energy. An optical fiber is a special type of waveguide that guides electromagnetic energy in the visible range by total internal reflection. In the integrated fluorescence sensing literature, the term waveguide has been used to refer to microfabricated light conduits. The principle of operation of both waveguides and optical fibers in fluorescence sensing is the same, i.e. the separation of fluorescence from excitation light is achieved in the same manner.

Quite a few researchers have used microfabricated waveguides to achieve separation of fluorescence from excitation light [16-18, 20, 34, 42, 130, 139-145] while several others have used optical fibers [28, 132, 134, 135]. There are two types of waveguide/fiber-based architectures in the literature. The first confines both the excitation and the fluorescence in the plane of the microfluidic channel as shown in Figure 8a). The second excites perpendicularly to the plane of the microfluidic channel and collects the fluorescence laterally through a waveguide as illustrated in Figure 8b). Alternatively, it is also possible to excite fluorophores in-plane and collect the fluorescence out of plane (Figure 8c).

Fabrication of these devices is typically achieved through soft lithography[†††]. However, the procedure is dictated by the choice of the substrate. Other machining techniques, such as wet and dry etching, can also be used.

The separation obtained using waveguide-based approaches is only partial. One can never position the waveguides in such a way as to achieve complete isolation between wavelengths. Therefore, these devices often require an off-chip filter or spectrometer to increase sensitivity.

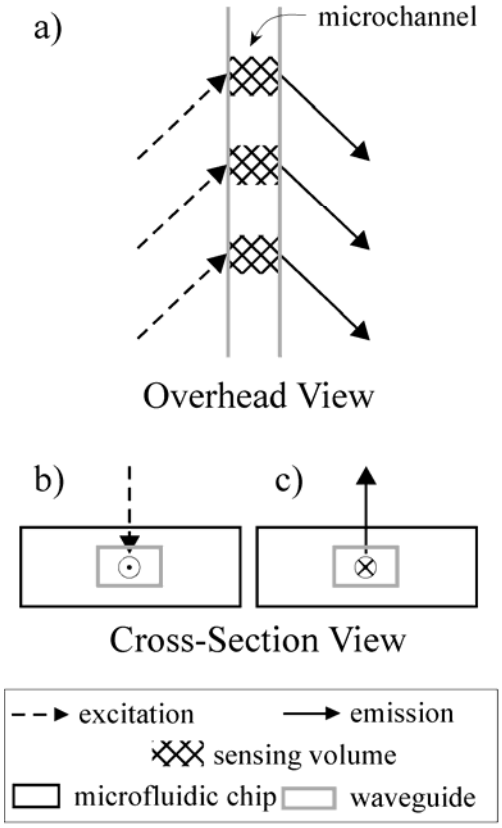

Figure 8. Sketch of geometries typically used in waveguide-based devices. a) Fluorescence and excitation are confined in-plane, but the fluorescence is collected at a different angle than the collimated excitation. b) Fluorophores are excited from the top, and fluorescence

[†††] Soft lithography is a micromachining technique utilizing soft materials (polymers).

is collected laterally (out of the page). c) Fluorophores are excited laterally (into the page) and fluorescence is collected perpendicularly.

6.3.2 Micro-Lenses

The concept behind the Roulet device [136-138] was combining illumination at an angle (geometry) with focusing by lenses (optics) to direct the excitation beam onto the sample and then away from the detector. The first set of lenses was placed on one side of a glass substrate containing microfluidic channels to converge the excitation beam onto the sample (Figure 9). The second set was placed on the opposite surface of the substrate, behind the channels, to deflect the excitation beam away from the photodetector. A fraction of the omnidirectionally-emitted fluorescence light reached the detector, which was on another substrate.

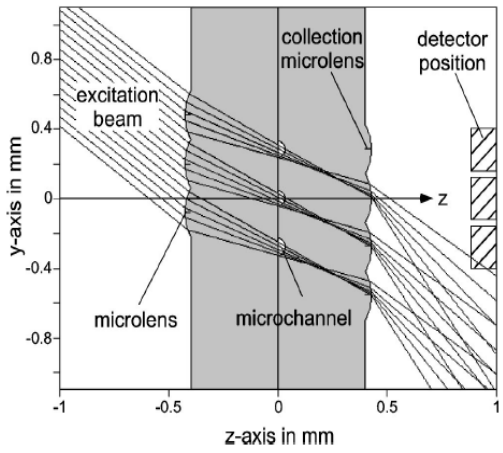

Figure 9. Cross-sectional sketch of a device based on free-space optical elements, showing a mechanism for separating fluorescence light from the excitation beam using lenses [137]. Photoresist lenses were microfabricated on the top and bottom faces of a glass substrate (gray) containing microfluidic channels, which run perpendicular to the page. Copyright Roulet et al. *Opt. Eng.*, 2001, 40**, 814-821.**

The microlenses were fabricated by patterning layers of photoresist on both sides of a previously micromachined Pyrex microfluidic chip. The chip was placed in an oven to melt the resist, which contracted into lens shapes by surface tension. The authors adjusted the process parameters to produce the desired focal lengths. Nearly 30% of the fluorescence light, the portion that heads into the substrate and toward the detector, was collected with this configuration; the detector yielded an SNR of 21 dB. The authors demonstrated the successful detection of 10 nM of the fluorophore Cy5.

6.3.3 Microfabricated Diffraction Gratings

Zeller et al. [134] demonstrated that filterless fluorescence could be realized with only a single grating. The fabrication of this device began with the fabrication of a mold by etching the grating pattern into a silica substrate and coating it with gold; this served as a mold for producing an electroplated nickel stamp. The resulting stamp was used to transfer the grating pattern onto a polycarbonate sheet. Subsequently, a titanium oxide waveguide was formed on the back side of the sheet, on top of the grating.

The operation of the device is illustrated in Figure 10. TM[‡‡‡] polarized light from a laser was coupled into the waveguide via the grating. Molecules adsorbed on top of the waveguide were illuminated by the TM mode of the laser beam's evanescent tail. The fluorescent light emitted by these molecules was coupled into TM and TE modes in the waveguide. These modes were again coupled out by the same grating, at different angles of diffraction for the different modes

‡‡‡ Transverse magnetic (TM) and transverse electric (TE) modes are solutions to Maxwell's equations which specify the intensity patterns of a propagating electromagnetic field. For TM modes there is no magnetic field in the direction of propagation, and for TE modes there is no electric field in the direction of propagation.

and wavelengths. The detector was placed at the diffraction angle for the TE mode of the fluorescent light in order to collect the fluorescence signal and not the excitation light from the laser, which appeared at the diffraction angle for the TM mode of the excitation light. The authors demonstrated the successful detection of 10 nM of Cy5-tagged species. No detection limit or SNR were reported.

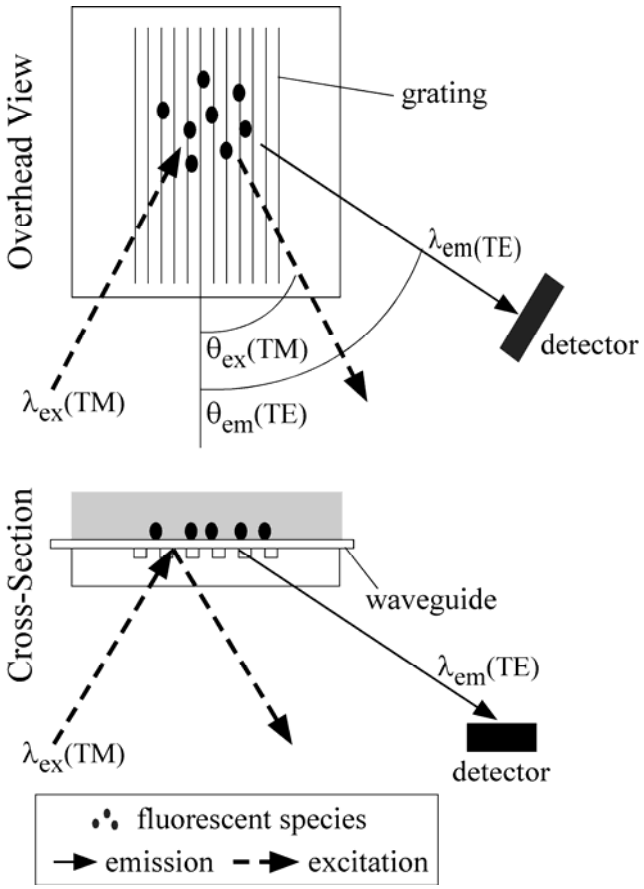

Figure 10. Polarized TM excitation light at wavelength λ_{ex} is incident at an angle θ_{ex}(TM) on fluorescently tagged molecules immobilized above a grating. The incident beam is diffracted through an angle $2\theta_{ex}$(TM), away from the detector, while the fluorescent emissions are coupled into the waveguide and diffracted out of the waveguide at an angle θ_{em}(TE) [134].

7 Summary of Achieved Device Performance

The performance metrics of the various miniature fluorescence sensors are summarized in Table 1. Two fundamental metrics are given when they were provided by the authors: the rejection and transmission levels[§§§] of the filters which we reported in decibels (on a $10\times\text{Log}_{10}$ basis). In the following two subsections, attractive features of each of the technologies are summarized based on their rejection and transmission levels, and then on the fabrication methods.

Reported detection limits are also included in Table 1: these indicate the performance of the devices in the assays for which they were designed. However, these figures cannot be used as a metric for comparison between sensors if the fluorophore is different, or in fact even if the fluorophore is the same since the emission intensity of the fluorophores depends on conditions such as pH and temperature. Therefore comparing sensors based on their detection limits is inappropriate unless care has been taken to reproduce exactly the same conditions.

[§§§] As previously mentioned, we are referring to the intensity of the light that is rejected/transmitted.

Table 1 . Performance synopsis for demonstrated miniaturized fluorescence sensors.

Filter Characteristics						Performance				References
Materials or Architecture	**Thickness (μm)**	**Excitation Wavelength (nm)**	**Emission Wavelength (nm)**	**Absorption Edge Location (nm)**	**Absorption Edge Width (nm)**	**Rejection (dB)**	**Transmission (dB)**	**Fluorophore**	**Detection Limit (nM)**	
Interference Only										
SiO_2 , TiO_2		490	515			-13	-1.05			Burns [5, 57, 62]
SiO_2, Si_3N_4		488	515	500	15	-20		fluorescein	85,000	Adams [58]
SiO_2 , TiO_2		530	580				-1	TAMRA	10,000	Kim [59]
SiO_2 , TiO_2	2.3	530	580			-30	-1	rhodamine 6G	1,000	Shin [64]
Absorption										
Poly-Si	1.5	365	450					NADH, DiFMUP		Iordanov [116]
Polycarbonate	80	360	510			-20	-1.05	fluorescein	25	Chabinyc [117]
Dye-Loaded PDMS	3000			560	30	-40	-1.6			Hofmann [119]
Ray Optics										
Micro-lenses	N/A			N/A	N/A			Cy5	3.3	Roulet [136-138]
Microfabricated Grating	N/A			N/A	N/A			Cy5	10	Zeller [134]
Waveguides and Fiber Optics	N/A			N/A	N/A			Cy5	24,000	Ruano [133]
Waveguides and Fiber Optics	N/A	635	650	N/A	N/A			Alexa Fluor 633		Powers [132]
Microprism	N/A	543		N/A	N/A			Cy3		Huang [35]
Orthogonal Geometry		540						Albumin Blue 580	1,200	Hofmann [129]
Spectrally Selective Detectors										
Photogate CMOS Pixel	N/A	470	520	N/A	N/A			SYBR Green	10,000	Maruyama [125, 126]
Multi-Wavelength III-V Detectors	N/A	371-651		N/A	N/A			fluorescein, chlorophyll, pyrene, GFP, RFP	2	Starikov [124]

Filter Characteristics						Performance				References
Materials or Architecture	**Thickness (μm)**	**Excitation Wavelength (nm)**	**Emission Wavelength (nm)**	**Absorption Edge Location (nm)**	**Absorption Edge Width (nm)**	**Rejection (dB)**	**Transmission (dB)**	**Fluorophore**	**Detection Limit (nM)**	
Filter + Ray Optics										
interference + directional source + lens		780				60**				Thrush [60, 61, 65-69]
bandgap absorption filter + directional source	1.2	475	510			-30*	-0.05*		120	Chediak [54]

* By our calculations. ** Best value is reported.

The most valuable feature of interference filters is the tailorability of the stopband, which can be placed in arbitrary ranges of the electromagnetic spectrum. Furthermore, their steep absorption edges allow the highest percentage of fluorescence photons to be collected and make this the only type of filter that can be used with fluorophores having small Stokes shifts. However, the angular sensitivity of their spectral characteristics may further limit their applications.

Semiconductor bandgap filters, on the other hand, have shown excellent rejection levels in the ultraviolet. While their non-zero absorption at fluorescent wavelengths is less than ideal for applications with low fluorescence intensity, it is preferable to the loss in sensitivity from insufficient rejection. The 2.4 μm CdS filter developed by Chediak et al. [54], for example, rejected the excitation light to -60 dB while still transmitting 40% of the fluorescence. For absorption filters in general, transmission levels are best for long Stokes shifted dyes.

Spectrally selective detectors also exploit the absorption characteristics of semiconductors, since they are a function of wavelength: the absorbance at energies above the bandgap increases monotonically with frequency. However, rejection is only moderate: -25 dB in experiments by Maruyama [125, 126] (this was demonstrated with LEDs rather than in fluorescence measurements).

It is clear that no one of these filtering approaches alone yields the high rejection in the stopband with the high transmission in the passband that will be necessary for the next generation of devices. There are two approaches to improving the performance. One its to combine interference or spectrally selective filtering with additional absorption filtering, as done in

Starikov [124]. Another is to combine these approaches with light separation methods that employ positioning, micro-optical elements, and/or light guiding to achieve the bulk of the rejection.

8 Proposed Performance Standards

In the interest of furthering progress in the field, we propose a set of performance standards for characterizing the spectral selectivity of miniaturized fluorescence sensors. Such metrics will permit the fair comparison of widely disparate approaches in order to allow better design of micro-fluorometers at the system-level for μTAS applications.

Fluorescence sensing systems can be divided into three parts: the optical components that determine how much of the excitation and fluorescence light falls on the area of the detector, the filter over the detector, and the detector itself. The overall performance of the sensing system is determined by the responsivity R and the noise N. Responsivity is a general term for an input-output characteristic, and in the case of photodetectors it has the specific meaning of the electrical output produced in response to a particular optical input intensity; which typically has units of A/W or V/W. The overall noise power N is the sum of photon shot noise and detector noise. The arrival of photons is a random Poisson process, so both noise power and signal-to-noise power ratio are proportional to the flux of photo-electrons in the detector. Photon noise sets a lower bound on the overall noise power [105].

The overall responsivity R of the system is the product of the detector responsivity with the composite transfer efficiency for the system components (defined in the following sections)

(1) $$R_{system}(\lambda) = R_{detector}(\lambda) * 10^{0.1*\left[H_{filter}(\lambda)+H_{geometry}(\lambda)+H_{loss}(\lambda)\right]}$$

where the responsivities are represented on a linear scale and the composite transfer efficiency is the sum of individual transfer efficiencies $H_x(\lambda)$, which are represented on a log scale as $10\log_{10}$(output intensity / input intensity) [****]. In order to allow comparison of different systems without reference to specific fluorophores, these responsivities and transfer efficiencies should be given as a function of wavelength.

At a minimum, if it is impossible to obtain these spectra, the responsivities and transfer efficiencies should be provided for the excitation and peak fluorophore emission frequencies. In the case that only the overall R_{system} can be obtained, $R_{system}(\lambda_{ex})$ and $R_{system}(\lambda_{em})$ can always be found using a standard procedure (section 8.5).

8.1 Detector Metrics

Since all detectors are spectrally selective, at least to a certain extent, the detector itself performs some spectral filtering. (This effect is exploited in the multi-wavelength spectrally selective detectors, section 5.) A metric that represents this phenomenon is the *quantum efficiency* (*QE*) of the detector, defined as the probability that an incident photon creates a photo-electron. The way in which each photo-electron contributes to the detector output signal varies according to the details of the detector; a metric that represents the overall conversion from incident photon to detector output is the responsivity $R_{detector}$, defined as the ratio between the electrical output

[****] The composite transfer efficiency would be the product of the individual transfer efficiencies if they were expressed on a linear scale, but it is the sum when expressed in dB.

signal and the incident optical intensity. The responsivity of the detector should be provided as a function of wavelength, $R_{detector}(\lambda)$.

(2) $R_{detector}(\lambda)$ = electrical output signal / incident optical power

There are standard methodologies for experimentally determining quantum efficiency and responsivity [147, 148]. The general approach to measuring responsivity is to provide a known optical intensity at a known wavelength as input to the detector and to measure the detector response. For different detectors the electrical output response may be in the form of voltage, current, or charge, which may be sampled using standard techniques. The optical intensity may be calibrated using another detector whose response is calibrated in the spectral range of interest. Because light beams diverge (i.e., increase in diameter) as they propagate, it is important to ensure that the distance between the light source and the detector remains the same for different measurements. In order to obtain reliable measurements it is also necessary to ensure spatial uniformity of the light source; for best results this is done using an integrating sphere[††††] but in many cases simple diffusers may be adequate. The intensity of the light source should be adjusted by setting the source at its maximum intensity and inserting neutral density filters into the light path rather than by using electronic controls, since in general the spectral characteristics of a light source vary with bias conditions.

Whereas quantum efficiency reflects the probability that an incident photon generates a photo-electron, responsivity reflects the overall conversion from optical input to electrical output. Thus

[††††] An integrating sphere is an optical component consisting of a hollow cavity with its interior coated for diffuse high reflectance, having relatively small holes for entrance and exit ports. It serves as an ideal diffuser, scattering and distributing incident light rays so that the outgoing light is spatially uniform.

the responsivity is the quantum efficiency multiplied by the internal gain of the photodetector. Typically, responsivity can be measured directly from the detector output, but determining quantum efficiency requires an estimate of the internal gain from generated photo-electrons to output response, which usually cannot be measured directly and must be estimated using statistical methods. Reviewing these methods is outside the scope of this paper, but they are detailed in [147, 148].

The minimum detectable signal is determined by the noise and is commonly taken to be the root mean square (RMS) noise, the square root of the noise variance. Signals in real detectors will be degraded by photon shot noise as well as noise sources including shot noise from bias currents, flicker noise (also known as $1/f$ noise), and thermal noise from thermal agitation of charge carriers. At low intensities, the noise is typically dominated by dark noise resulting from leakage currents in the detector [112]. Ideally, the power spectral density of the detector noise should be provided as a function of both temporal frequency and intensity [149]. The RMS noise is the square root of the spectral density integrated over all temporal frequencies and can be determined from measurements of the detector output using standard techniques [150]. The power spectral density can be measured using a spectrum analyzer, and the RMS noise can be estimated as the standard deviation of an ensemble of samples of the output signal from the detector. At a minimum, the RMS noise $\sigma_{detector}(I)$ as a function of input intensity I should be provided (under the assumptions that the detector is a linear system, and that detection is performed using a single measurement with no temporal filtering or signal modulation). In order to allow comparison of different systems without reference to temporal filtering and signal modulation strategy, the

power spectral density of the detector noise should be provided as a function of temporal frequency f and intensity, $N_{detector}(f,I)$.

8.2 Filter Metrics

Table 1 shows that few authors report the characteristics of the filters used in their systems. We recommend that such information always be provided by reporting the transmission spectrum of the filter. This is an important design parameter that allows one to estimate the performance of a micro-fluorometer with a wide variety of fluorophores. In addition, it allows devices to be categorized by their transition wavelengths and their rejection and transmission levels.

Because it is difficult to discern variations in low-transmission regions in spectra reported in linear units or from absorption coefficient data, transmission measurements should be reported in decibel units. As mentioned previously, this has not been the norm, since in other fields absorption spectra have traditionally been reported in a variety of other units. For detecting low fluorescence levels, however, it is necessary to distinguish levels below -20 dB, such as between -30 and -50 dB, which appear as zero on a linear scale. Also, the dB representation better shows the passband to stopband transitions than does the absorption coefficient (Figure 5a).

The transfer efficiency of the filter is equal to its transmission, given by

$$H_{filter}(\lambda) = T(\lambda) = 10\log_{10}\left(\frac{I(\lambda)}{I_0(\lambda)}\right), \tag{3}$$

where $I(\lambda)$ is the intensity of light (μW/cm^2) after filtering and $I_o(\lambda)$ is the intensity of light incident on the filter.

The absorption edge or cutoff wavelength λ_c and the absorption edge width w define the transition between stopband and passband. The former determines the excitation sources and fluorophores that can be employed, while systems with large w are restricted to use with fluorophores that have large Stokes shifts. The standard definition for λ_c for an electronic long-pass filter is the wavelength at which the transmission is -3 dB. The upper frequency limit of the passband is defined as a given fraction of λ_c, and the stopband is defined as the frequency range for which the transmission is less than a specified arbitrary value, such as -20 or -40 dB. However, these definitions are problematic for optical filter transmission spectra, which do not have the ideal characteristics illustrated for a long-pass filter by the dashed line in Figure 1, and which do not have specified roll-off slopes but varying slopes that we wish to characterize.

We propose an algorithm that determines the absorption edge and the absorption edge width from measured data. The technique extends to all types of optical filters. The absorption edge λ_c is specified as the wavelength at which the first derivative of the transmission spectrum is maximized. The absorption edge width is specified as the full width at half maximum (FWHM) of the first derivative. Thus, the lower and upper limits of the absorption edge width, λ_s and λ_p, are the wavelengths on either side of λ_c at which the first derivative is half of its maximal value (in dB). These definitions are illustrated in Figure 11 and Figure 12, in which these procedures have been applied to data from absorption and interference filters. The definitions of absorption edge λ_c, absorption edge width w, and transmission and rejection levels T_{pb} and T_{sb} are described by the following equations.

(4) $$\lambda_c \equiv \arg\max_{\lambda} \frac{dT(\lambda)}{d\lambda}$$

$$\frac{dT(\lambda_s)}{d\lambda} \equiv \frac{1}{2}\max_{\lambda} \frac{dT(\lambda)}{d\lambda} \qquad \lambda < \lambda_c$$

$$\frac{dT(\lambda_p)}{d\lambda} \equiv \frac{1}{2}\max_{\lambda} \frac{dT(\lambda)}{d\lambda} \qquad \lambda > \lambda_c$$

$$w \equiv \lambda_p - \lambda_s$$

$$T_{sb} \equiv T(\lambda_s)$$

$$T_{pb} \equiv T(\lambda_p)$$

However, these computations are problematic when the curve is not smooth. Under these circumstances it may be necessary to apply a smoothing operation to the data prior to computing the derivative. For example, a 5-point smoothing average was performed on the transmission data shown in Figure 11. Smoothing should be kept to a minimum, since it artificially broadens the spectrum.

If the system has multiple filtering stages (i.e. from packaging materials such as PDMS), their individual as well as cumulative responsivities should ideally be provided. Note that $H_{filter}(\lambda)$ may be somewhat different for the excitation and fluorescent light, since the they travel through different optical paths in the system. For example, sometimes a spectral filter is placed in the excitation light path in order to restrict the spectral bandwidth of the excitation light, so that this filter is included in H_{filter} for the excitation light, but this additional filter is irrelevant for the fluorescent light because it is not positioned between the sample and the detector. After the sample, the spectral filtering is identical for both.

8.2.1 Absorption Filter Spectra

For absorption filters, it is difficult to specify the absorption edge location and width from absorption coefficient spectra (Figure 5). Absorption coefficients typically decrease monotonically as the wavelength increases, never reaching zero and with variations in the slope. This is true for the spectrum of CdS (Figure 5 a), to which the proposed algorithm is applied in Figure 11 (computed from the absorption coefficient spectrum using the Beer-Lambert law for a hypothetical 1 μm film). The top panel shows the transmission spectrum alongside computed locations of the edge and edge width, and the bottom panel shows the first derivative from which these metrics were obtained. The wavelength at which the first maximum occurs in the first derivative is the absorption edge λ_c. The half-maximum wavelengths define the boundaries, and thus the width, of the absorption edge.

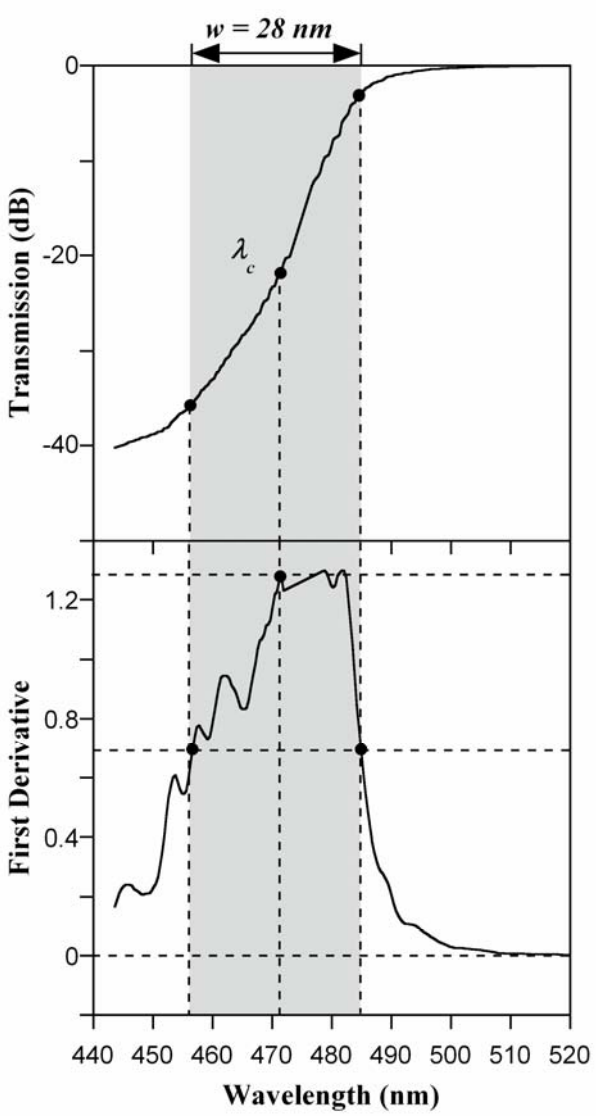

Figure 11. a) The transmission spectrum of a 1 µm thick CdS film. The solid circles and shaded region indicate the absorption edge width *w* and cut-off wavelength λ_c. b) The application of the FWHM technique to the first derivative of the transmission spectrum (in dB).

8.2.2 Interference Filter Spectra

Interference filters often have large ripples in the transmission band (Figure 2), with peak-to-peak ripple heights that can be tens of percent. The ripple positions are highly sensitive to

fabrication variations, so using absolute criteria such as magnitude (i.e., -3 dB) to define absorption edge location and width might arbitrarily shift these values by tens of nm. In Figure 12, our suggested algorithm has been applied to the transmission spectrum for a 1.2 μm silicon nitride/silicon dioxide interference filter.

Thus far the absorption edge has been specified by a single wavelength λ_c for one stopband-passband pair, but interference filters or micromachined fluorescence sensors for multi-wavelength spectroscopy would have several absorption edge locations. In this case the definition of absorption edge and absorption edge width may be extended to describe the multiple wavelengths $\lambda_{c1}, \lambda_{c2}, \lambda_{c3}, \ldots$ and widths w_1, w_2, w_3,… associated with the stopbands and passbands of the system. These wavelengths may be specified using the same algorithm, applied in different spectral bands to capture all the absorption edges and absorption widths of the system.

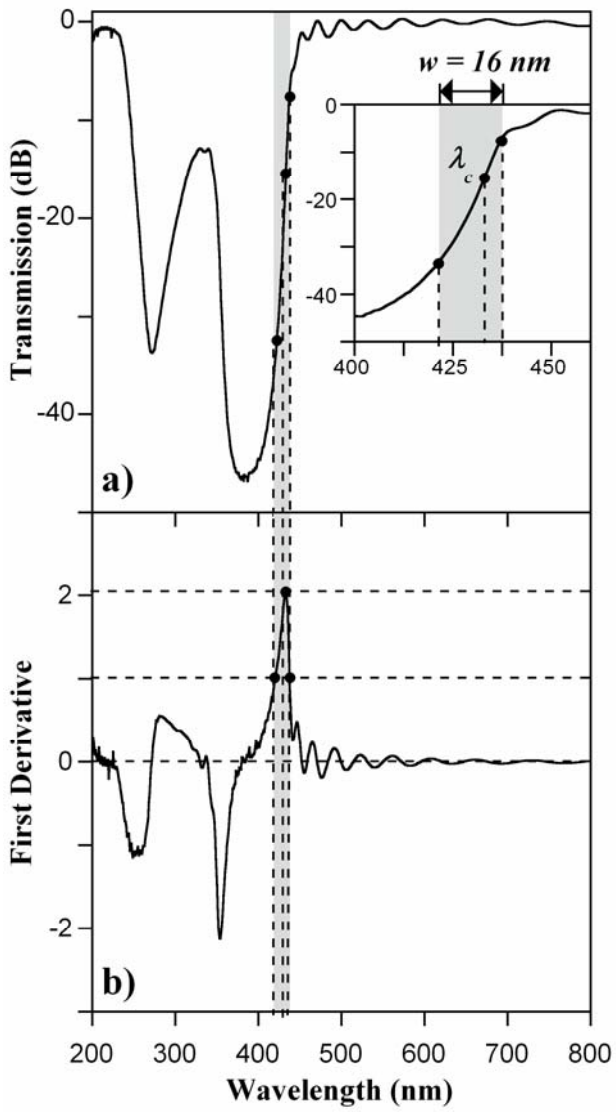

Figure 12. a) The transmission spectrum of a 1.2 µm-thick interference filter. The solid circles and shaded region indicate the absorption edge width *w* (shaded region) and cut-off wavelength λ_c. The inset shows a finer view of λ_c and *w*. b) The application of the FWHM technique to the first derivative of the transmission spectrum (in dB).

8.2.3 Single Number Metrics

Using the proposed technique, passbands and stopbands can be explicitly determined. Therefore we suggest that the following single-number metrics be reported for the filter if the entire transmission spectrum cannot be obtained: 1) the rejection in the stopband at λ_{ex},

$$T_{sb} = 10\log_{10}\left(\frac{I(\lambda_{ex})}{I_0(\lambda_{ex})}\right) \tag{5}$$

and 2) the transmission in the passband at λ_{em}, T_{pb}, defined analogously. Although this will not allow comparison of the filter with those in other systems, it will give an indication of the effectiveness of the filter with a particular fluorophore.

In addition to providing the ability to easily determine the filter metrics, the FWHM method also provides the capability to quantitatively compare the absorption edges of different systems. We define the attenuation factor γ (dB/nm) associated with an absorption edge as the measure of the rate of change of transmission at that edge. This metric is computed by dividing the change in transmission across the transition between passband and stopband by the absorption edge width.

$$\gamma = (T_{sb} - T_{pb}) / w \tag{6}$$

For example, the attenuation factor of the interference filter in Figure 12 is γ = 1.6 dB/nm, whereas the attenuation factor for the CdS filter in Figure 11 is γ = 1.1 dB/nm. Although this metric does not offer any insights on the absolute rejection and transmission levels around that edge, it does allow the designer to determine the relative rejection and transmission levels near the edge. This is particularly important when designing systems to detect emissions from fluorophores having small Stokes' shifts. Note that the attenuation factor γ as defined above (in dB/nm) is distinct from the transmission loss (typically expressed in dB/cm). Although the units

are similar, the former quantifies the steepness of an optical filter's absorption edge whereas the latter is commonly used to denote the magnitude of transmission across material of a given thickness.

8.3 Optical Path Filtering: Coupling Efficiency

The optical part of the fluorescence sensor also requires metrics equivalent to transmission, rejection, and absorption edge location and width, since the prevalent SNR metric not only incorporates the detector performance, but also the brightness of the sample, and is thus an extrinsic rather than intrinsic quantity.

The optical path of the sensor system includes the placement of the detector relative to the light source, free-space optical elements such as lenses, and light-guiding components. For these, metrics such as λ_c and w may be ambiguous. Instead, the optimal wavelength for the device should be provided together with the range of usable wavelengths.

Ideally, curves showing the fraction of light falling on the detector as a function of wavelength should be provided for both the excitation light source and the fluorescent probes. This may be difficult in practice. In order to quantify the collection efficiency, we adapt the notion of *coupling efficiency* (CE), which is widely used in fiber optics to denote the efficiency of power transfer between two optical components. We quantify geometrical effects on collection efficiency by defining coupling efficiency as the fraction of light that is able to impinge on the detector area. This analysis should be performed for the excitation light source in order to quantify the degree to which the photodetector is shielded from excitation light and for light

emitted by the fluorophores in order to quantify what fraction of the emitted fluorescence is able to fall upon the photodetector. The CE can be employed as a design tool to maximize collection of emitted fluorescence and to minimize collection of excitation light.

For the optical path filtering, the transfer efficiency in dB is given by

(7) $$H_{geometry,ex}(\lambda) = 10\log_{10}\left[CE_{ex}(\lambda)\right]$$

(8) $$H_{geometry,em}(\lambda) = 10\log_{10}\left[CE_{em}(\lambda)\right]$$

for the excitation light and fluorescent emissions, respectively. Ideally, the CE should be given as a function of wavelength, but if this is not possible the CE should be determined for the excitation and peak fluorophore emission wavelengths. Note that the optical path filtering is inherently different for excitation light and fluorescent light, since the two sources of light travel through different optical paths in the system.

8.3.1 CE for Fluorescence Light

For emitted fluorescence, the system geometry factor quantifies geometrical effects on collection efficiency that result from differences in the fraction of the total solid angle received by the detector. Typically fluorescence is emitted isotropically, so the solid angle of emission is 4π. The maximum solid angle subtended by a planar detector is 2π, which occurs for the special case of a detector that is large and in direct contact with the sample. Design constraints might not allow positioning of the detector in such proximity, and in many cases the solid angle subtended by the detector is significantly less than 2π.

If the system has lenses to collect or redirect the light, as in Figure 4, their effects should be included in the CE. In the case of collection, focusing increases the amount of fluorescent light impinging on the detector, so the CE is greater than that for the detector alone. For the ideal case of a lens that focuses all the light falling on it onto the detector, the solid angle subtended by the lens may be taken as the effective detector area. (It may be possible to collect emissions from more than 2π of the total solid angle using reflective surfaces, but this has not yet been demonstrated for a micro-fluorometer.)

The CE can be determined for any system geometry. For generality, we define a function Q which represents the relative light intensity as a function of the angular spherical coordinates θ and ϕ. The function Q is normalized so that

$$\int_0^{2\pi}\int_0^{\pi} Q(\theta,\phi,\lambda)\sin\phi\, d\phi\, d\theta = 4\pi\,. \tag{9}$$

For the special case of a fluorescent point source with isotropic emission, the fluorescence intensity is constant: $Q(\theta,\phi,\lambda)=1$.

The fluorescence CE is the ratio between the fluorescent photons impinging on the detector and the total number of fluorescent photons emitted, given by:

$$CE_{em}(\lambda) = \frac{\iint_{\Omega_d} Q(\theta,\phi,\lambda)\sin\phi\, d\phi\, d\theta}{4\pi} \tag{10}$$

where Ω_d is the solid angle subtended by the detector.

Determining the fluorescence CE is straightforward for fluorescent point sources with circular or square detectors (Figure 13), which are the most commonly used. For an ideal circular detector centered at $\phi = 0$, the polar angle α subtended by the detector is related to the detector diameter a and distance d to the fluorophores via a trigonometric relation:

$$\alpha = 2\cos^{-1}\left(\frac{d}{\sqrt{\frac{a^2}{4}+d^2}}\right) \tag{11}$$

The solid angle subtended by the detector is then given by:

$$\int_0^{2\pi}\int_0^{\frac{\alpha}{2}} \sin\phi d\phi d\theta = 2\pi\left[1-\cos\left(\frac{\alpha}{2}\right)\right] = 2\pi\left[\frac{\sqrt{\frac{a^2}{4}+d^2}-d}{\sqrt{\frac{a^2}{4}+d^2}}\right] \tag{12}$$

The fluorescence CE for this detector is thus:

$$CE_{em} = \frac{1-\cos\left(\frac{\alpha}{2}\right)}{2} = \frac{\sqrt{\frac{a^2}{4}+d^2}-d}{2\sqrt{\frac{a^2}{4}+d^2}} \tag{13}$$

This function exhibits the expected asymptotic behavior, since $CE_{em} \xrightarrow[\alpha\to\pi]{} 1/2$, $CE_{em} \xrightarrow[a\to\infty]{} 1/2$, and $CE_{em} \xrightarrow[d\to 0]{} 1/2$.

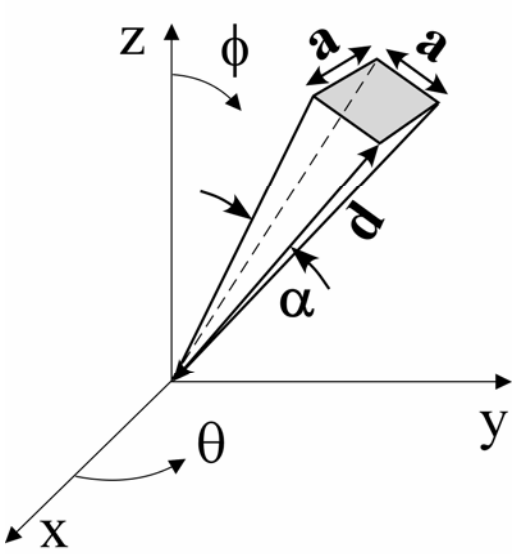

Figure 13. Solid angle α for emission from a fluorophore located at the origin and intercepting a square detector a distance d away with an area as indicated by the gray shading.

Likewise, the fluorescence CE for an ideal square detector centered at $R = d$, $\phi = 0$ with side length a is:

$$CE_{em} = \frac{\alpha}{2\pi}\sin\left(\frac{\alpha}{2}\right) = \frac{a}{2\pi\sqrt{\frac{a^2}{4}+d^2}}\cos^{-1}\left(\frac{d}{\sqrt{\frac{a^2}{4}+d^2}}\right) \tag{14}$$

This function exhibits the same asymptotic behavior.

The fluorescence CE can just as readily be calculated for more complex geometries. For the case of an annular detector (such as in Figure 4), the CE is found by subtracting the CEs of two circular detectors with radii equal to the inner and outer diameters of the ring.

8.3.2 CE for Excitation Light

For excitation light, the coupling efficiency quantifies geometrical effects on rejection that result from differences in the fraction of excitation light that reaches the detector. For the excitation light, the function *Q* (equation (9)) would be replaced by the emission intensity *I*, which would not generally be isotropic but would depend on position (excitation light is usually directional) and wavelength.

The excitation CE is the ratio between the excitation photons reaching the detector and the total number of photons from the excitation source, given by:

$$CE_{ex}(\lambda) = \frac{\iint_{\Omega_d} I(\rho,\theta,z,\lambda)\ \rho\ d\rho\ d\theta\ dz}{\iint_{\Omega_{4\pi}} I(\rho,\theta,z,\lambda)\ \rho\ d\rho\ d\theta\ dz} \tag{15}$$

where Ω_d is the solid angle subtended by the detector, $\Omega_{4\pi}$ is the total solid angle, and the excitation intensity is defined in cylindrical coordinates due to its directionality.

Most lasers emit beams that have a Gaussian profile. A Gaussian beam has a time-averaged intensity given by

$$I(\rho,z) = I_0\left(\frac{w_0}{w(z)}\right)^2 \exp\left(\frac{-2\rho^2}{w^2(z)}\right) \tag{16}$$

where ρ and *z* denote the axial and radial location of the detector in polar coordinates, $w(z) = w_0\sqrt{1+\left(\frac{z}{z_0}\right)^2}$ is the beam width, and w_0 is the radius of the beam waist which occurs at

$z = 0$ [151]. For an ideal circular detector of diameter a positioned at the center of a Gaussian beam, this leads to a CE_{ex} of:

$$CE_{ex}(\lambda) = 1 - \exp\left[\frac{-a^2}{2w^2(z)}\right] \tag{17}$$

This function exhibits the expected asymptotic behavior, since $CE_{ex} \xrightarrow[a\to\infty]{} 1$, and $CE_{ex} \xrightarrow[z\to\infty]{} 0$. Similarly, the CE_{ex} for an ideal square detector of diameter a positioned at the center of a Gaussian beam is:

$$CE_{ex}(\lambda) = \mathrm{erf}\left(\frac{a}{\sqrt{2}w(z)}\right)^2 \tag{18}$$

Again, this function exhibits the expected asymptotic behavior, since $CE_{ex} \xrightarrow[a\to\infty]{} 1$, and $CE_{ex} \xrightarrow[z\to\infty]{} 0$.

8.4 Optical Path Losses

In real optical systems, additional losses will play a role in determining overall system performance. In a full description of the optical path of the system, absorption and scattering would have to be taken into account, as would focusing and numerical aperture effects. For example, two types of scattering commonly occur for the excitation light: large angle scattering due to sidewall roughness of a waveguide and small angle scattering due to interaction of the excitation light with the sample itself [1]. Both can result in unwanted excitation light falling on the detector. Also, the intensity of the fluorescence light will be attenuated as it is scattered and absorbed by materials within the system before it reaches the detector. Numerical aperture comes into play because when light exits a waveguide, it expands in the lower index of refraction

medium, which would most typically be air or water. This may reduce the amount of light reaching the sample, which will reduce the excitation light as well as fluorescent light hitting the detector. These effects are difficult to model accurately, so H_{loss} will usually be determined experimentally, and will represent a correction to the other components of the composite transfer efficiency and overall system responsivity as given in equation (1).

For optical path losses, the transfer efficiencies in dB are given by

$$H_{loss,ex}(\lambda) = 10\log_{10}\left[\frac{I_{ex}(\lambda)}{I_{ideal,ex}(\lambda)}\right] \tag{19}$$

for the excitation light and

$$H_{loss,em}(\lambda) = 10\log_{10}\left[\frac{I_{em}(\lambda)}{I_{ideal,em}(\lambda)}\right] \tag{20}$$

for the fluorescent emissions. Ideally, $H_{loss,ex}$ and $H_{loss,em}$ should be given as a function of wavelength, but if this is not possible then they should be determined for the peak excitation and emission wavelengths of the fluorophore. Note that the optical path losses are inherently different for excitation and fluorescent light, since the two may travel through different optical paths in the system. The optical losses are expected to increase transmission in the stopband and decrease transmission in the passband, reducing the overall sensitivity of the fluorescence measurement.

8.5 Minimal System Metrics and Calibration

It is clear from the preceding discussion that the overall performance of a micro-fluorometer depends on many factors. For fair comparison of widely disparate approaches, it is necessary to quantify the effects of each of these factors separately, as functions of wavelength and intensity.

However, it may not be practical or possible to carry out such exhaustive analysis and empirical characterization.

A minimal set of system metrics that should be reported if it is impossible to obtain the metrics described above are $R_{system,em}(\lambda_{em})$, $R_{system,ex}(\lambda_{ex})$, and $\sigma_{detector}$ (see section 8.1) as functions of incident intensity Γ. $R_{system,ex}(\lambda_{ex})$ represents the overall system response to light at the excitation wavelength, with the input optical intensity determined at the input to the micro-fluorometer (or at the light source if the light source is part of the micro-fluorometer). The reference location for calibration of excitation intensity is therefore at the input to the system. The input intensity can be determined by placing a reference optical detector, which has been calibrated at the excitation wavelength, at the same position with respect to the light source as the micro-fluorometer. (This may not be feasible in the case of an integrated light source, in which case a free-standing version of the same light source should be used.) The distance from the light source to the calibrated detector should be the same as in the standard measurement configuration, and the optically sensitive area of the reference detector should be matched to the optically sensitive area of the micro-fluorometer (or the measured intensity should be adjusted to account for any differences). The intensity of the light source should be adjusted using neutral density filters rather than electronic controls, as described above.

$R_{system,em}(\lambda_{em})$ represents the overall system response to light at the peak emission wavelength, with the input optical intensity being the fluorescence intensity. (Note this system metric includes the effects of all the component metrics, such as the fluorescence CE.) Fluorescence intensity depends on the absorbance and quantum yield of the fluorophore as well as the intensity

of the excitation light, and absorbance, in turn, depends on the molar extinction coefficient and concentration of the fluorophore as well as the optical path length through the sample. For dilute solutions and low excitation intensities, fluorescence intensity is proportional to each of these parameters. At higher concentrations and intensities, the relationship becomes nonlinear due to effects such as self-absorption, quenching, and photobleaching. Both the molar extinction coefficient and the quantum yield are sensitive to environmental conditions.

The reference location for calibration of fluorescence intensity is inside the sample chamber. The purpose is to calibrate what the detector reads in response to a particular fluorescence intensity. There are three alternative strategies for calibration of the intensity: calibration from the input of the system to the sample chamber, or calibration from the sample chamber to the output of the system, and use of a calibrated fluorophore. The choice of which method to use depends primarily on the relative difficulty of modifying the micro-fluorometer for the desired measurement.

The first method is useful for any micro-fluorometer. A reference light source with calibrated intensity at the peak emission wavelength is placed at the same position with respect to the detector as the sample chamber, and the output of the detector is monitored. This may be accomplished by modifying a representative micro-fluorometer so that the reference light source can be placed in the appropriate location (i.e., in the sample chamber).

The second method requires two measurements, which are combined to calibrate the intensity. The first measurement is the responsivity of the detector alone for a reference light source at the

emission wavelength, with the intensity calibrated at the detector. The other measurement is the transfer efficiency of the micro-fluorometer between specific locations within the system. A calibrated light source at the peak emission wavelength is applied at the input to the system. The intensity is measured, using a reference optical detector that has been calibrated at the emission wavelength, at two places: with the detector in its usual position, and with the detector placed at the same position with respect to the light source as the sample chamber. This may be accomplished by modifying the micro-fluorometer so that the reference detector can be placed in the appropriate location (i.e., in the sample chamber). Dividing the source-detector responsivity by the source-chamber responsivity gives the transfer efficiency between chamber and detector, then multiplying the detector responsivity by this chamber-detector transfer efficiency accounts for losses in the optical path between the sample chamber and the detector.

Finally, a third option for calibrating the fluorescence intensity is the use of a calibrated fluorophore solution. The National Institute of Standards and Technology has developed a method to quantify fluorescence radiance in terms of *molecules of equivalent soluble fluorophores* (MESF). NIST provides a standard reference solution (SRM 1932) of fluorescein with well-controlled pH and concentration for quantification of fluorescence intensity. Unfortunately, the technique has been developed only for fluorescein, so assays with other fluorophores require reference solutions to be prepared in-house. For details on the MESF quantification of fluorescence, refer to [152, 153]. There are, however, several difficulties with this method. First, the *fluorescence quantum yield*, which is the number of fluorescence photons emitted per incident excitation photon, varies significantly with changes in the microenvironment, so great care must be taken to ensure that the pH and temperature of the

reference solution are matched to the system under test. Second, it is well known that the quantum yield of a fluorophore varies, depending on whether it is dissolved in solution, immobilized on a surface, or conjugated to a biological specimen.

9 Conclusions

A wide variety of spectral discrimination schemes have been demonstrated, but none has been established as a paradigm for miniaturized fluorescence sensors. This is a consequence of the trade-offs between performance and complexity. For more demanding applications in which the fluorescence signal is weak, some increase in complexity is inevitable since none of the current technologies can be used alone; a combination of methods will be required to increase sensitivity while also achieving strong rejection of the excitation light.

The micro-scale fluorometers that have been demonstrated to date work well with high brightness samples. The challenge for the next generation of devices is improving the sensitivity so that these systems can accomplish low-light tasks such as single-molecule detection. This will require more attention to the filter performance than has been paid so far, including device design and fabrication details, as well as the measurement of the metrics achieved by the various device components. Without such metrics, it is impossible to compare the widely disparate approaches in order to improve overall system design and performance.

Collection efficiency also needs to be considered if detection of single molecules is to be achieved in μTAS. The issue of collecting more of the fluorescent light using optical elements

has not yet been addressed. Furthermore, no systems have been made that focus the totality of the emitted light onto the detector to increase the signal strength.

Although it can be argued that monolithic integration of all the components is desirable for achieving the highest reliability and smallest size, it is usually not possible and may come with too high a cost in terms of fabrication complexity, individual component performance, and system design constraints. As can be seen from this review, none of the reported devices has integrated light source, detector, and microfluidics all on one substrate. Some of the devices integrated the microfluidics, filter, and detector, but could not integrate the light source due to the device configuration [5, 57, 62]. Alternatively, the light source, filter, and detector were integrated, and the microfluidics were placed off-chip [54]. The latter configuration allows the device to be reused by simply replacing the microfluidic network. In addition, using a ray-optics based microsystem with no integrated light source [134, 136-138] offers versatility: the system is not constrained to any particular light source and can therefore be used with any fluorophore. Integration choices will thus continue to be influenced by the intended device application.

Acknowledgements

We would like to thank Dr. Miao Yu, Dr. Marc Cohen, Dr. Andreas Andreou, and our colleagues in the Laboratory for MicroTechnologies and the Integrated Biomorphic Information Systems Laboratory for helpful discussions and exchanges on the material presented in this paper. Also, we would like to thank Dan Hinkel for fabrication of the interference filters. We acknowledge Great Lakes Chemical Corp. for providing the chromophore used in our experiments. Financial

and logistical support for this work were provided by the National Science Foundation and the Laboratory for Physical Sciences.

Chapter 3: Spectral Responsivity Characterization of an Integrated Fluorescence Sensor Comprising a CMOS Photodetector and a Custom Polymeric Optical Filter

Abstract

We report the design and experimental results from an integrated fluorescence sensor. The sensor is comprised of a novel differential active pixel sensor (APS). Spectral responsivity measurements revealed a maximum sensitivity at 490 nm. The sensor was fitted with an ultraviolet-blocking high-rejection polymer filter and its spectral responsivity was measured. The filtered chip revealed a maximum rejection of nearly -20 dB at 370 nm.

1 Introduction

Fluorescence-mediated assays offer both sensitivity and selectivity when compared to other imaging techniques used in biochemical analysis. In the past two decades, there has been a growing interest in harnessing the benefits of fluorescence sensing at the microscale in order to provide additional capability to micro-(total analysis systems) (μ-TAS). A great number of miniature bio-sensors that use fluorescence sensing as a detection modality have been reported in the literature [6]. However, the performance of these devices still lags that of their macroscale counterparts because of poor signal-to-noise ratio (SNR). Two factors result in degraded SNR: first, the effectiveness of spectral discrimination techniques does not scale with device size and second, the noise floor of the solid state detectors is too high for detecting typically weak fluorescent signals. The sensor is a low-noise CMOS sensor fabricated in a 0.5 μm technology and is designed to minimize environmental noise at the expense of slight increase in reset noise.

The operation of this sensor and its noise rejection mechanism are not discussed in this thesis[‡‡‡‡]. Rather, we focus on the design of high rejection optical filter and assess for the performance of the *integrated* sensor (filter + detector) by characterizing its spectral responsivity.

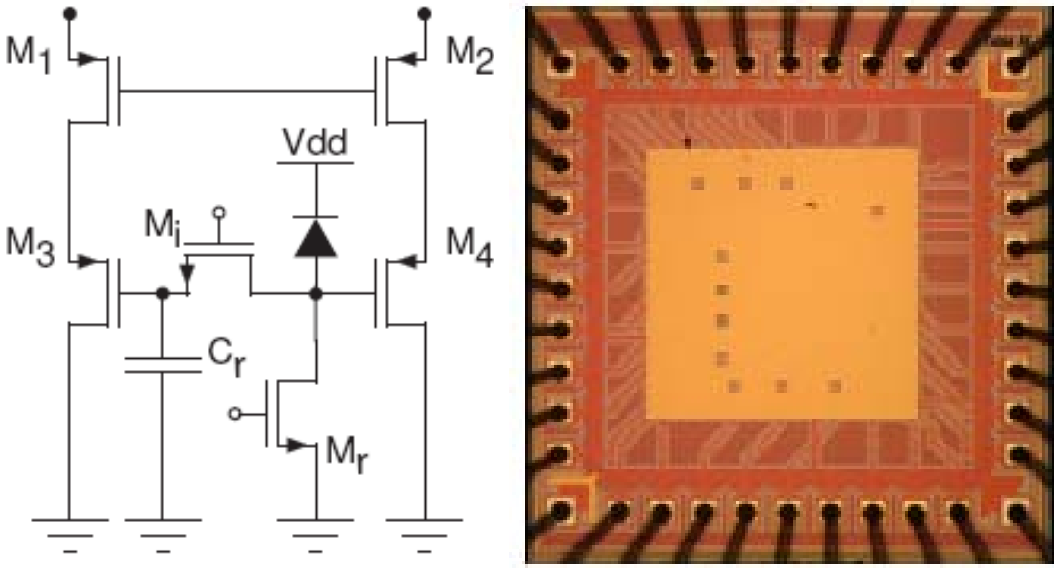

Figure 14. Circuit architecture (left) and chip photomicrograph (right).

As a filtering material, we developed a microscale organic absorption filter designed for high-sensitivity integrated ultraviolet fluorescence spectroscopy. We aimed for the following features: first, the filter should be as thin as possible (between 1 and 50 μm); second, it should reject as much of the ultraviolet excitation light as possible while transmitting fluorescent wavelengths with nearly zero transmission loss; and third, the filter should be patternable. These features are desired in order to facilitate integration without compromising performance.

The demonstrated filter consists of a polymer matrix doped with the ultraviolet-absorbing chromophore *(2)-2-hydroxy-methyl-phenyl-benzotriazole*, hereinafter BTA. Loading of

[‡‡‡‡] For details on these matters please consult ref. [31] D. Sander, M. Dandin, H. Ji, N. Nelson, and P. Abshire, "Low-noise CMOS fluorescence sensor," presented at IEEE Int. Symp. Circuits and Systems (ISCAS07), New Orleans, LA USA, 2007.

chromophores in polymer matrices has previously been demonstrated in integrated fluorescence spectroscopy [119] and other applications [107, 111-115], but one of original contributions stemming from this work is that the filters are made out of polymers that can be microstructured with *standard ultraviolet photolithography* and/or *dry etching*.

2 Filter Fabrication

The chemical structure of BTA is shown in Figure 15 and its absorption spectrum in Figure 16. Benzotriazoles[§§§§] are an important class of UV-absorbers. Their main use has been for polymer stabilization [154], protecting plastics from degradation in sunlight. The mechanism of their UV-absorption is reported in ref. [154].

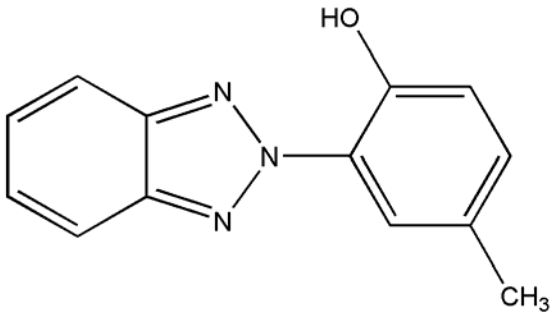

Figure 15. Molecular structure (2)-2-hydroxy-methyl-phenyl-benzotriazole.

[§§§§] The complete name of the chemical family is *2-hydroxybenzotriazoles* [154] R. E. Lee, C. Neri, V. Malatesta, R. M. Riva, and M. Angaroni, "A new family of benzotriazoles: how to modulate properties within the same technology," in *Specialty Polymer Additives*, S. Al-Malaika, A. Golovoy, and C. A. Wilkie, Eds. Cornwall: Blackwell Science, 2001.

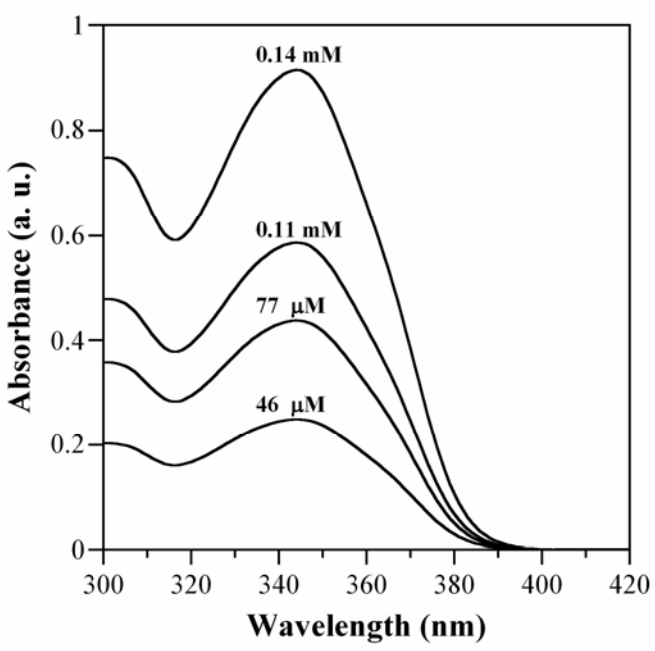

Figure 16. Chromophore (dissolved in toluene) absorption in the UV regime. Absorption at wavelengths longer than 400 nm is negligible.

The host polymers were chosen for integration and functional purposes. They were EPON SU-8 50 (Microchem Corp.) and the acrylic Humiseal 1B66 (Chase Corp.). SU-8 is commonly used in microfabrication, and its ability to be photopatterned will allow selective placement of filters in an integrated platform. The acrylic polymer is typically used for protecting electronic circuits from moisture and environmental contamination. It was chosen because of its reported low moisture uptake[*****]. We have developed a custom dry-phase etching procedure for patterning it, to also allow selective placement in integrated platforms.

The fabrication of the filter consisted of physically mixing the chromophore with the polymer precursor, the monomer in the case of SU-8, and in the case of 1B66, in the diluted phase of the

[*****] A total-analysis system, as shown in Chapter 2, often comprises microfluidic channels. The polymers used to make these channels should have low water uptake in order to maintain the system's structural integrity.

polymer. Specific fabrication sequences for each type of filter are described below. Desired filter thicknesses were achieved using spin-coating. The spin curve for the acrylic was experimentally determined and is shown in Figure 17. The same material is available from the manufacturer for SU-8 50. (Adding the chromophore did not affect this spin curve.)

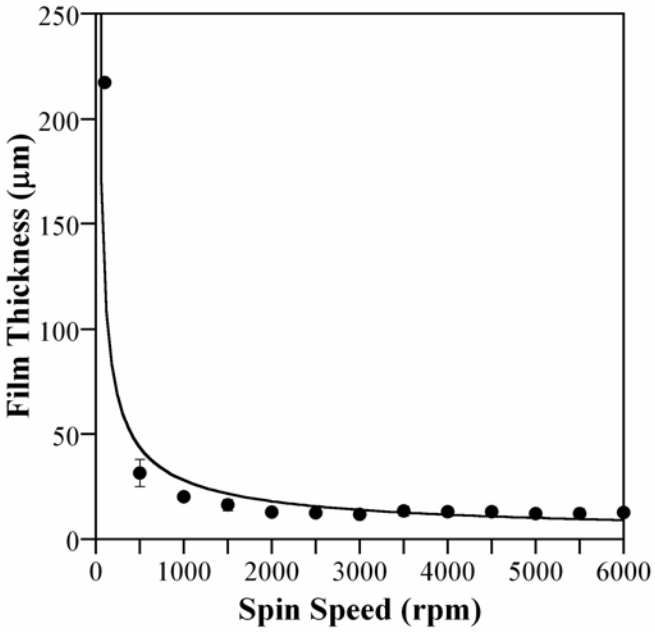

Figure 17. Spin curve of 1B66-BTA composites.

2.1 1B66 Filters

Fabrication began by adding the desired amount of chromophore to a fixed volume (10 mL) of diluted polymer. Note that 1B66, as it comes from the manufacturer, is dissolved in methyl-ethyl-ketone and toluene. We have determined, in additional experiments (data not shown), that both solvents are highly favorable for BTA dissolution.

For low-loading concentrations, the mixture was agitated until total dissolution[†††††] was achieved between the chromophore and the polymer precursor. For high loading concentrations, a

[†††††] The extent of the dissolution was assessed by visual monitoring.

homogenizer was used to speed up dissolution. Solvent extraction to form the solid films was achieved by placing the samples in a fume hood for 48 hours. (It should be mentioned that the polymer remains soluble in these solvents thereafter and that assays using these solvents cannot be performed with 1B66-based filters.) Alternatively the solvents were extracted using a thermal cycle (90 °C on a hotplate for 10 minutes). However, this was done at the expense of film uniformity.

2.1.1 Dry-phase patterning of 1B66 Films

Patterning of 20 μm-thick 1B66 filters was achieved using oxygen plasma dry etching. Two types of samples were prepared. The first consisted of samples patterned with thick (7.5 μm) photoresist masks[‡‡‡‡‡], and the second of samples patterned with aluminum hard masks.

Patterning was successful with both methods. However for thicker films, the photoresist mask eroded, before the complete removal of the filter, due to a faster etch rate. Aluminum etch masks are therefore preferable, as is shown in Figure 18a. Subsequent removal of the aluminum mask via chemical stripping was found to be compatible with the filter (Figure 18c).

[‡‡‡‡‡] SPR-220 7.0 (Shipley Corp.)

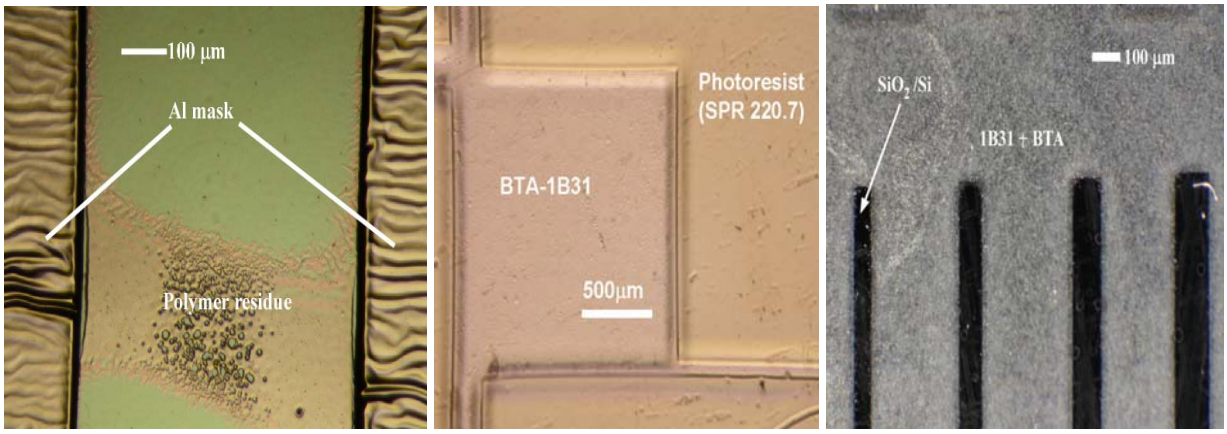

a) **b)** **c)**

Figure 18. a) An aluminum mask for etching a space between the two lines. The picture shows polymer residue left after incomplete etching. b) Patterned 1B31 loaded with the chromophore after stripping the Al mask. c) A film patterned using the photoresist mask.

2.2 SU-8 Filters

The general fabrication sequence for the SU-8 filters was as follows. The desired quantity of chromophore powder was added to 10 mL of SU8-50 monomer. The mixture was stirred thoroughly using a homogenizer at 280 rpm for 10 minutes. The mixture was then dispensed on the substrate and spun at using the appropriate spin-cycle for obtaining a 50 μm thickness. The substrate was baked on a hotplate at 65 ^{o}C for 2 minutes. The temperature was then ramped to 95 ^{o}C at a rate of 300 ^{o}C/hour and held at that temperature for 30 more minutes. The sample was exposed to ultraviolet radiation at a dosage of 2160 mJ/cm^2 at 405 nm (g-line lithography). The same thermal cycle was then performed to complete the photochemical reaction.

2.2.1 Photolithographic Patterning of SU-8 Based Filters

If the host material is broadband-sensitive (i.e. absorbs light over of a wide range of wavelengths), wavelengths that lie outside the absorption band of the chromophore can be used to cure the filters. We demonstrated this concept using the negative photoresist SU-8 50. Typically, SU-8 lithography is done at 365 nm (i-line) because it has stronger absorption at that wavelength. However, it is also possible to cure SU-8 films using g-line (405 nm) exposure. Because benzotriazoles have virtually zero absorption at 405 nm, the ultraviolet light needed to cure the host material is not absorbed by the chromophore.

Ultraviolet curing of UV-absorber/polymer composites has been shown previously [155]. However these authors used wavelengths that lie *in* the absorption band of the chromophore. This means that both the photoactive compound of the polymer and the UV-absorbing compound compete for the incident photons. Curing is still possible; however, the recipe must be changed for different concentrations of chromophore. Therefore, the advantage of curing the polymer composite with wavelengths that lie outside the absorption band of the chromophore is a concentration-independent procedure.

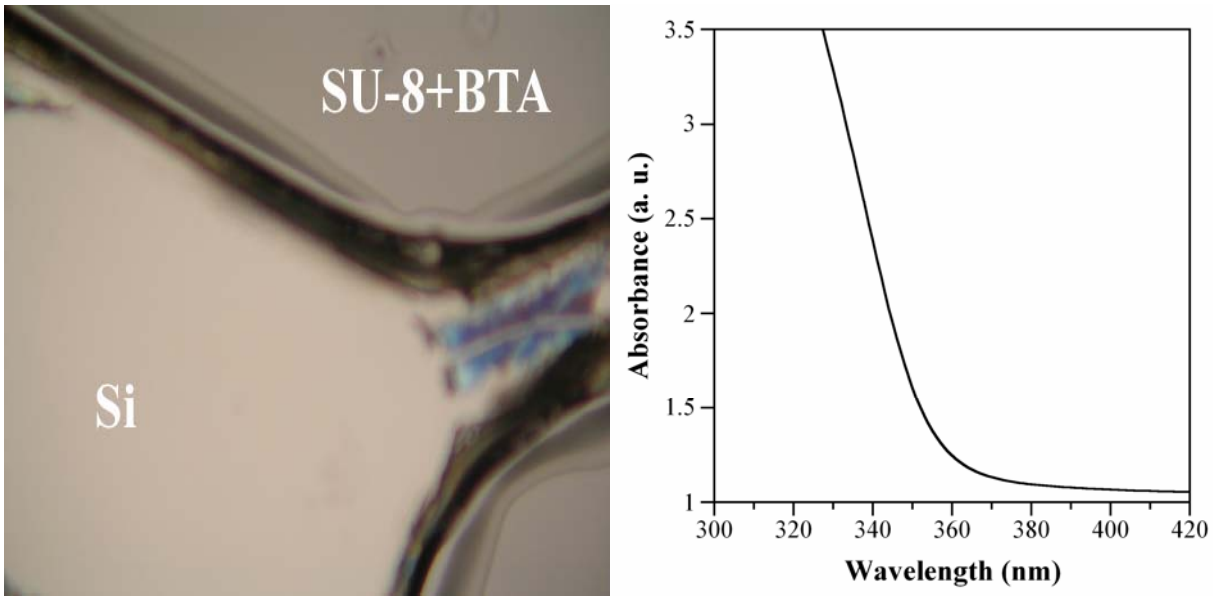

Figure 19. A microchannel patterned in SU-8 (50 μm thick) (left) and transmission spectrum of composite film (right).

3 Integrated Sensor Characterization

Because of packaging concerns[§§§§§], a thin film-filter was not integrated with the photodetector chip. Unlike SU-8, 1B66 can be cast in thick films with moderate uniformity and does not require UV exposure for curing. Therefore, we used the 1B66-based filters in order to establish the proof-of-concept of an integrated CMOS/MEMS hybrid sensor. A picture of the polymeric film cast onto the CMOS die (the photodetector chip shown in Figure 14) is shown in Figure 20. In the remainder of this chapter, we characterize the integrated sensor for its spectral responsivity in order to assess its performance for UV-fluorescence assays. Responsivity is a metric which relates the detector's output to its input. It is an overall measure of the conversion of incident

[§§§§§] The CMOS chip are packaged in a DIP40 ceramic enclosure and are routed to I/O leads using wire bonds. This arrangement makes contact photolithography difficult, as would be needed in the case of SU-8.

photons to photo-generated charge and in the case of a charge mode (QM) pixel such as the one shown in Figure 14, has units of V $s^{-1}W^{-1}$.

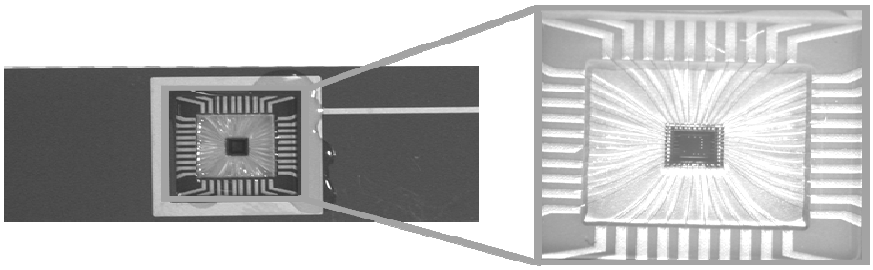

Figure 20. Polymeric filter (1B66) cast onto the CMOS chip. The filter was loaded with a medium level concentration of chromophore (1 mM in the polymer precursor) in order to a yield a homogenous film

4 Instrumentation for Spectral Responsivity Characterization

The sensor was characterized using the setup shown in Figure 21a. A grating monochromator (Newport Cornerstone 260 1/4M, model 74100) was used to provide wavelengths ranging from 330 to 800 nm with a spectral resolution of 1 nm, achieved utilizing 280 μm wide slits (Oriel 77217). The monochromator comprises a blazed grating (350 nm) (Newport 260i) mounted on a computer-controlled turret and a set of mirrors which focus the broadband light source from a 200 W Hg-Xe lamp (Newport 6292) onto the grating and the diffracted spectral components onto the exit slit.

The spectrum of the lamp is shown in Figure 21b. Desired optical intensities were obtained by placing a neutral density filter of appropriate optical density at the output of the monochromator. The light exiting the filter was then directed into an integrating sphere for spatial equalization. The intensity of the light was measured using a calibrated photometer head (Newport 818-UV) fitted with a 5 mm diameter pinhole and an optical power meter (Newport 1830-C). All

measurements were taken at an ambient temperature of 28°C. The output signal from the chip was acquired using a PC-based data acquisition system. The data acquisition software worked in synchrony with software used to control the monochromator and record optical power. Control and acquisition software were all written in Matlab 7.2.0 (Mathworks, Inc.) and Labview 8 (National Instruments Inc.).

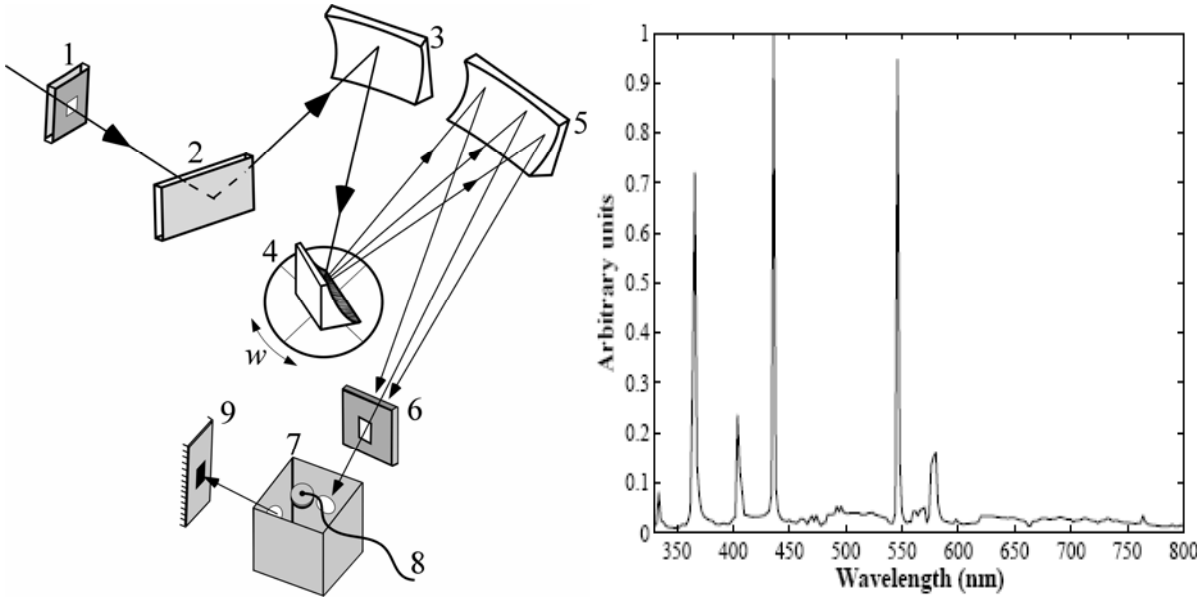

a) **b)**

Figure 21. a) The monochromator comprised slits (1, 6), mirrors (2, 3, and 5), and a grating (4). Additional components used were: a neutral density filter (not shown, but typically placed between 6 and 7), an integrating sphere (7) and a calibrated photometer head (8). The integrated sensor is placed at the output of the integrating sphere (9). b) Spectrum showing the relative magnitudes of the intensities arising from the Hg-Xe lamp.

5 Results

Sensor output voltage traces (such as the one shown in the top panel of Figure 22) were collected for 2 seconds under various illumination conditions (wavelengths ranging from 330 nm to 800 nm). An average of 500 traces was computed for each illumination condition. A Matlab program was written in order to estimate the slope ($V\ s^{-1}$) of the resulting trace, in order to compute the responsivity ($V\ s^{-1}W^{-1}$) of the photodetector. The slope was divided by the optical power incident on the photodiode assuming no reflective losses at the chip surface. The optical power incident on the chip was obtained by scaling the power density obtained from the calibrated photometer by the photodiode active area.

An important result is obtained from computing the slope of the output traces. It was found, as is well known, that the slope of the output trace was not constant over the period in which the sensor is not saturated (0 to 1.3 seconds on the top panel of Figure 22). This is due to the varying capacitance as the photodetector integrates the photo-generated charge. This means that the responsivity is not constant in time. However, since typical assays only require an endpoint voltage reading [156], the responsivity curves shown in Figure 23 were computed by taking an average responsivity. To do so, the output trace was partitioned, from start to finish, into 600-point long data segments. The slopes of these segments were computed and are plotted in the bottom panel of Figure 22. The slope used for the responsivity was computed over the region indicated by the double-arrow bar. Computing the responsivity in this region offered the best possible estimate since, in the regions excluded in the calculation, the sensor is either in a transient state following reset or saturated due to the accumulation of the photo-generated charge on the integration capacitance.

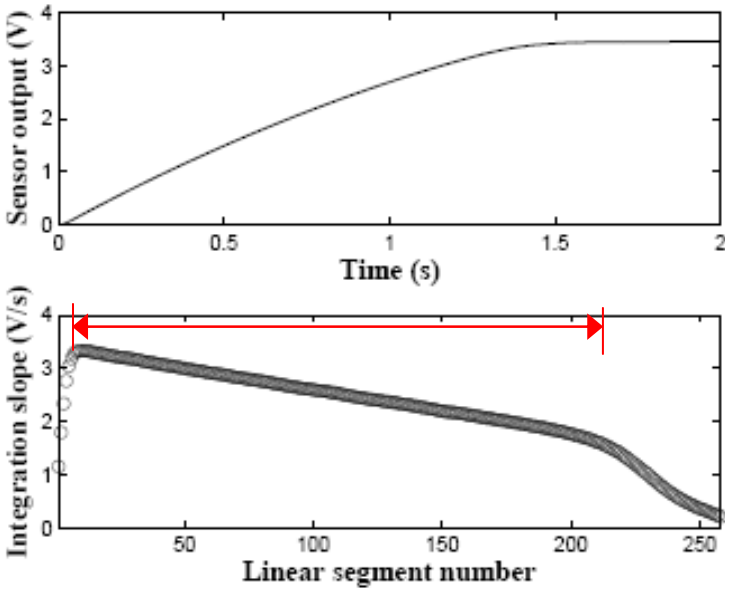

Figure 22. Top panel: Sensor output as a function of time. Bottom panel: this figure shows the non-linearity of the slope as a function of time of the linear segment number.

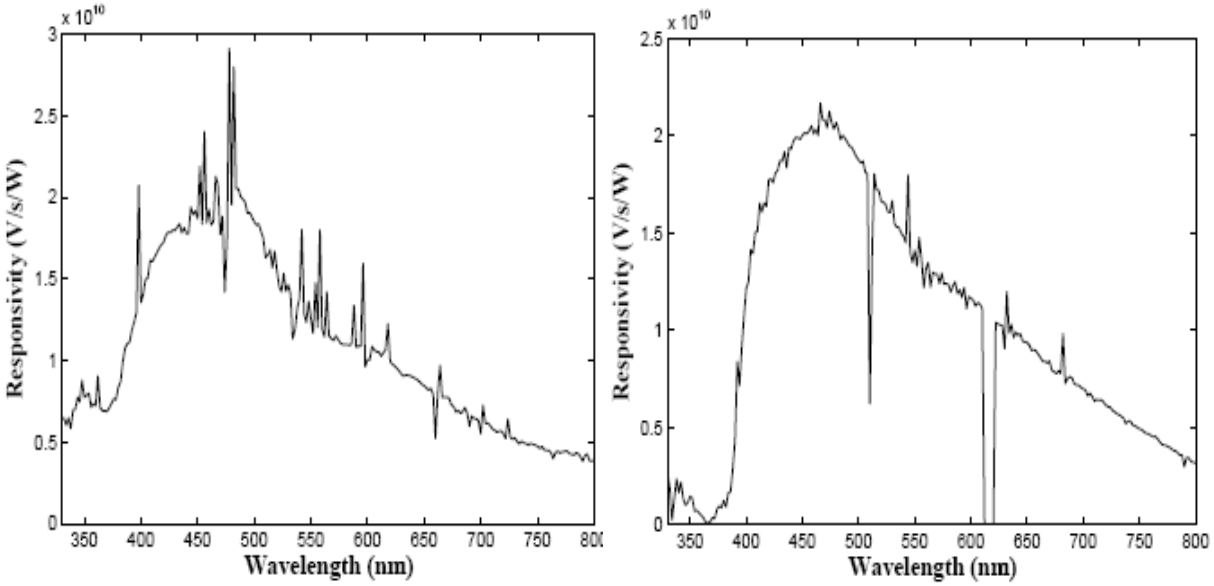

Figure 23. a) Responsivity spectrum of an unfiltered chip. B) Responsivity spectrum of the filtered chip.

6 Discussions and Conclusions

As Figure 23 shows, the detector is less sensitive from 300 to 400 when the filter is cast onto it. This is strong evidence that the filter material is attenuating wavelengths in that range, preventing impinging photons from eliciting an appreciable response. The maximum rejection was found to be ~ -20 dB and occurs at 370 nm. This rejection level is in contrast with the spectrophotometric data which showed that the transmission of a 20 µm-thick spin-cast filter (on a glass slide) produced a maximum rejection of -30 dB (at 375 nm) for the particular concentration used (1 mM in the polymer precursor). Nevertheless, the sensor was still able to detect small concentrations of fluorophore (20 nM of free Calcium concentration in an assay with calcium) [31]and monitor real time metabolic activity of yeast cells (*Saccharomyces cerevisiae*) through the detection of autofluorescent nicotinamide adenine dinucleotide (NADH) [156].

7 Materials and Methods

7.1 Photolithography and Patterning

Optical lithography of SU-8 filters was conducted using the g-line channel (405 nm) of an MJB3 Karl Seuss contact mask aligner. A reactive ion etcher (Trion Inc) was used to pattern the 1Bxx films, which were masked with SPR 220 7.0 photoresist (Shipley Corp.) that had been exposed at 365 nm and developed in CD-30 (Microchem). Aluminum masks were deposited by thermal evaporation (Metra Corp.), and patterns were defined using photolithography with 1813 photoresist (Shipley Corp.) and CD-30 (Shipley Corp.) developer.

7.2 Metrology

The transmission spectra of test samples were collected, in reference to air, using a Cary 5000 UV-VIS-NIR spectrophotometer (Varian Inc.). All scans were performed from 800 nm to 300 nm at 1 nm increments. The light source change-over point was located at 350 nm. The scan rate was 600 nm/min, and a 2 nm spectral bandwidth was used. The slit height was set to full. All spectra were baseline-corrected in order to subtract the contribution of the cover slips.

A Dektak 3ST (Vecco, Inc.) mechanical surface profiler was used for measuring the thickness of the cured films. A groove was cut in the films down to the substrate using a razor blade to produce a step for the profile. A total of 5 samples were measured to obtain an average film thickness.

Chapter 4: Single Photon Avalanche Diodes in Standard CMOS[******]

Abstract

We report an improved design and successful demonstration of single photon avalanche diode (SPAD) detectors fabricated in a standard nwell 0.5 μm CMOS technology. The detectors are implemented as circular junctions between p+ and nwell regions. Two techniques are used to suppress perimeter breakdown: guard rings at the edges of the junctions, formed using lateral diffusion of adjacent nwell regions, and a poly-silicon control gate over the diffused guard rings and surrounding regions. The detectors exhibit a breakdown voltage of -16.85 V, ~4 V higher than simple diode structures in the same technology. The detector exhibits a thermal event rate of 16000 counts/s at room temperature at an excess bias voltage of 1.15 V.

1 Introduction

Photon counting devices are useful for detecting very weak light or quickly decaying optical signals. Typically photomultiplier tubes are used in photon counting applications. Though they have high detection efficiency, they are large and fragile and require high voltages (~1000V) for operation. As a result they offer limited possibilities for system integration. For this reason, several authors[157-161] have tried to implement comparable avalanche detectors using solid state devices.

[******] [7] M. Dandin, N. M. Nelson, V. Saveliev, I. Weinberg, H. Ji, and P. Abshire, "Single Photon Avalanche Detectors in Standard CMOS," in *6th Annual IEEE Conference on Sensors*. Atlanta, Georgia, 2007.

The avalanche mechanism in silicon is mediated by impact ionized electron hole pairs. When a reverse bias voltage higher in magnitude than the breakdown voltage is applied across a p-n junction, thermally generated or photon-generated electron-hole pairs are accelerated by the high electric field present in the depletion region and generate secondary pairs by impact ionization. The newly generated carriers are in turn accelerated, causing more impact ionization, and thus giving rise to the well-known avalanche phenomenon.

This effect is exploited in single photon avalanche diode (SPAD) detectors. Once the avalanche mechanism is triggered, however, the device cannot sense subsequent events until the avalanche current has been quenched. The onset of avalanche accurately matches the arrival time of a photon. Quenching lowers the voltage across the diode below its breakdown voltage, eliminating the breakdown required for the avalanche mechanism and preventing any subsequent avalanche events. Following this cycle, the voltage across the junction is raised above the breakdown voltage and avalanche can occur once again.

Thus far, SPADs have been made through dedicated processes in order to achieve desired characteristics. However, there is increasing interest in porting their fabrication to mainstream CMOS processes [131]. This would lead to enhanced performance by allowing their integration with other mixed-mode circuits. CMOS SPADs will also pave the way to higher levels of integration and reduced cost by replacing bulky photomultiplier tubes. This will allow the implementation of low cost positron emission tomography (PET) scanners and enable novel applications such as PET-guided surgery[162] and the detection of extremely fast fluorescence decays in lab-on-a-chip (LOC) applications.

One of the main challenges of SPAD design in standard CMOS processes is premature breakdown at the perimeter of the diode. This reduces the active area of the device and results in poor photon detection efficiency. In this paper we report novel structures using two techniques to eliminate perimeter breakdown: a guard ring technique previously reported in [160] in combination with an original control gate method described in this paper. The remainder of this paper is organized as follows. First, we describe the detector architecture and the techniques used for suppression of premature breakdown. A description of the circuit and experimental setup follows. Finally, measured characteristics of the device are provided along with results from the detector in a fluorescence titration experiment.

2 Suppression of Perimeter Breakdown

As mentioned above, the primary challenge in implementing SPAD devices using standard CMOS processes is to suppress the premature breakdown that occurs at the perimeter of the diode due to surface effects. A common method used to prevent edge breakdown in SPADs is the implantation of guard rings on the perimeter of the diode to reduce strong electric fields [160]. In standard nwell processes, however, it is not possible to implement guard rings for p+/nwell junctions due to the absence of a low-doping p-well layer. Rochas et al. suggested using the inevitable lateral diffusion between adjacent nwells to achieve a lower doped region at the edges of the devices. This is achieved in physical layout by placing adjacent nwell regions at or below the minimum suggested spacing for the technology, which results in a more lightly

doped n-type region in between the two wells. This reduces the electric field strength and suppresses breakdown in this region.

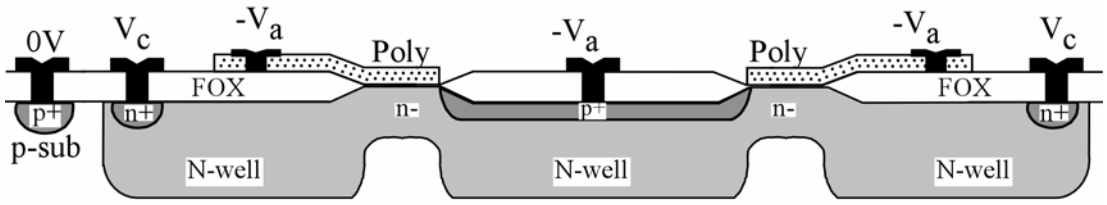

Figure 24. Cross-sectional view of the SPAD device. Lateral diffusion of two adjacent nwells creates a lighter doped region at the edges of the junction (n-regions), and a poly control gate further depletes the surface.

We introduce an original method for breakdown suppression as well: the addition of a poly-silicon control gate which further depletes the surface at the edge, again reducing the electric field strength and suppressing breakdown. We have designed, fabricated, and characterized novel structures which use both methods to achieve improved breakdown characteristics (Fig. 1).

Simple diodes and diodes with guard rings but no control gates were also fabricated for comparison. Suppression of edge breakdown was confirmed by increased breakdown voltage (-16.85 V) relative to simple diodes without guard rings or control gates (-12.5 V), and to diodes with guard rings but no control gates (-14.75 V).

3 Circuit Operation

The circuit shown in Fig. 2 was used for readout. The anode and the control gate were both held at -18 V which corresponds to an excess bias voltage -1.15 V. The excess bias voltage is defined

as (Va – Vbreakdown) and is an important parameter in SPAD design. The avalanche current was quenched using an off-chip resistor. Once breakdown occurs, the avalanche current is dissipated through the 35 k resistor. This effectively reduces the voltage across the diode. In order to accurately characterize rise times without artifacts in the output trace, the readout voltage was buffered using a high slew rate amplifier (4100 V/μs). Fig. 3 shows a typical output trace from the device, where each spike corresponds to a quenched avalanche event. The rise time of the avalanche pulse was measured to be 5 ns, while the decay time following quenching was 2 us and the full width at half maximum (FWHM) was 500 ns.

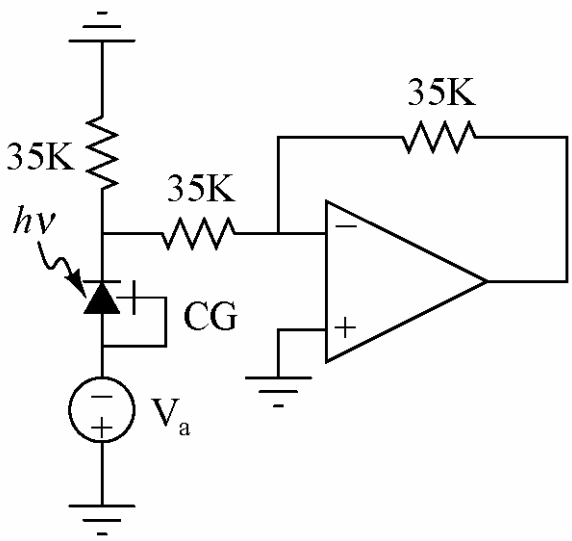

Figure 25. Readout circuit architecture. The control gate (CG) and the anode are held at the same potential. All resistors and the amplifier are off-chip.

4 Instrumentation

In order to determine the detector's count rate under various conditions, a LABVIEW (National Instruments) program was developed to estimate the mean time between triggers of the data

acquisition card. The time differences between triggers were tallied into a histogram, and the mean time was determined. The count rate is the reciprocal of the mean time between triggers. A sample histogram is shown in Fig 4. A monochromatic (510 nm) light beam with a spectral resolution of ±1 nm was obtained using a grating monochromator (Cornerstone 260, Newport Stratford Inc.). To adjust the optical power of the beam, neutral density filters were used at the output port of the monochromator. An integrating sphere was used to spatially equalize the beam to ensure a uniform optical power distribution on the detector. One of the output ports of the sphere was fitted with a calibrated photometer head for optical flux measurements. The output voltage from the circuit was acquired using a PC-based data acquisition system.

For the fluorescence sensing experiment, a custom test fixture was attached to the output port of the monochromator. The fixture comprised a compartment for placing a cuvette containing the solution under study and a slot for placing a commercial emission filter.

5 Measured Characteristics

In order to determine the detector's count rate under various conditions, a LABVIEW (National Instruments) program was developed to estimate the mean time between triggers of the data acquisition card. The time differences between triggers were tallied into a histogram, and the mean time was determined. The count rate is the reciprocal of the mean time between triggers. A sample histogram is shown in Fig 4. A monochromatic (510 nm) light beam with a spectral resolution of ±1 nm was obtained using a grating monochromator (Cornerstone 260, Newport Stratford Inc.). To adjust the optical power of the beam, neutral density filters were used at the

output port of the monochromator. An integrating sphere was used to spatially equalize the beam to ensure a uniform optical power distribution on the detector. One of the output ports of the sphere was fitted with a calibrated photometer head for optical flux measurements. The output voltage from the circuit was acquired using a PC-based data acquisition system.

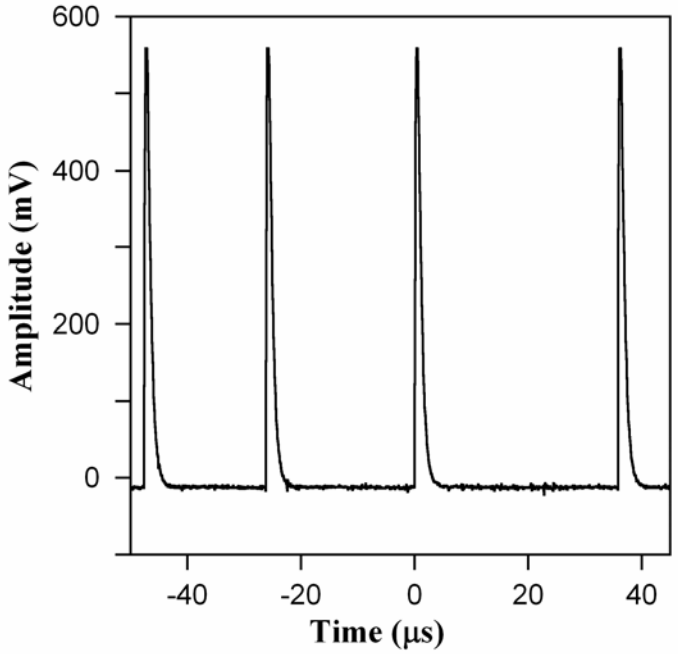

Figure 26. Four successive avalanche events with a timing resolution of 500 ns.

For the fluorescence sensing experiment, a custom test fixture was attached to the output port of the monochromator. The fixture comprised a compartment for placing a cuvette containing the solution under study and a slot for placing a commercial emission filter.

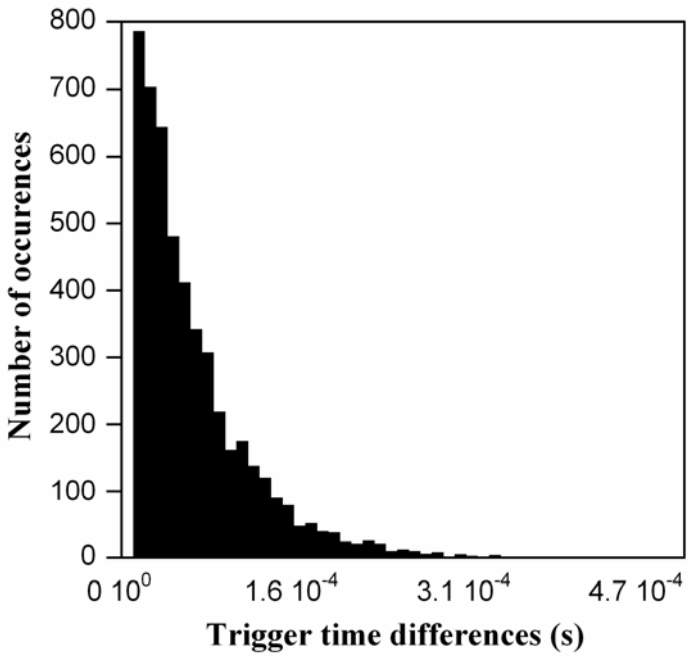

Figure 27. Sample histogram of trigger time differences used to estimate mean count rate.

5.1 Dark Count

Even in the absence of light, avalanche events occur spontaneously due to thermally generated electron-hole pairs or to charges released from traps following an avalanche event. These events result in a nonzero "dark count." The dark count was determined for various excess bias voltages; at an excess bias voltage of 1.15 V, the dark count is 16000 count/s (c/s) at room temperature. The dark count increases rapidly with increasing excess bias voltage, as shown in Fig. 5. This behavior is expected because higher excess bias voltages widen the depletion region and thus the avalanche volume. Moreover, carriers may also be generated using field assisted mechanisms, which give rise to additional dark pulses in a voltage-dependent fashion.

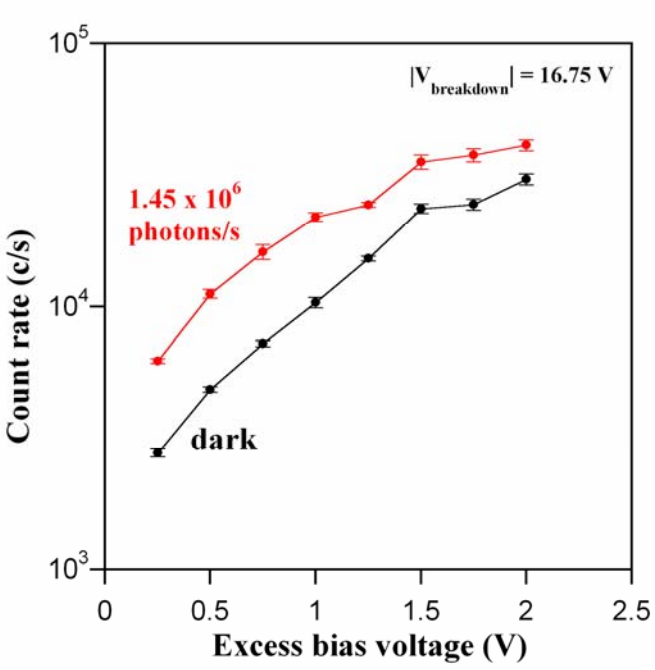

Figure 28. Detector response in the dark and under high illumination intensity as a function of excess bias voltage.

5.2 Responsivity to Light

Neutral density filters were used to obtain four orders of magnitude of incident light intensity (106-102 photons/s). Over this entire incident intensity range, the count rate exceeded the dark count by at least one standard deviation. (Fig. 6).

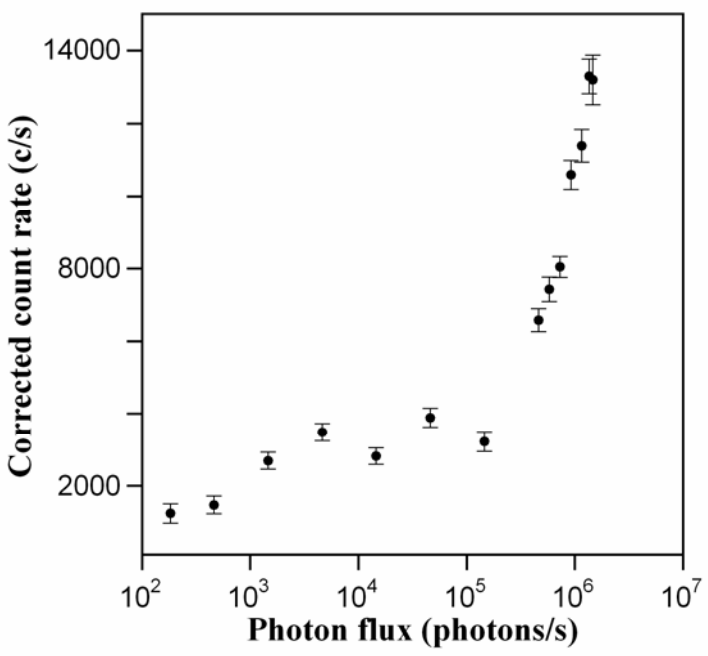

Figure 29. Detector response as a function of incident illumination intensity. The optical power was adjusted using neutral density filters.

5.3 Inferred Quantum Efficiency

The inferred quantum efficiency at 510 nm was estimated by computing the ratio of the observed count rate to the photon flux. This was done for a range of incident intensities as shown in Fig 7. The experiment revealed that the detector exhibits extremely high quantum efficiency at low incident intensities, whereas efficiency is significantly degraded at high incident intensities.

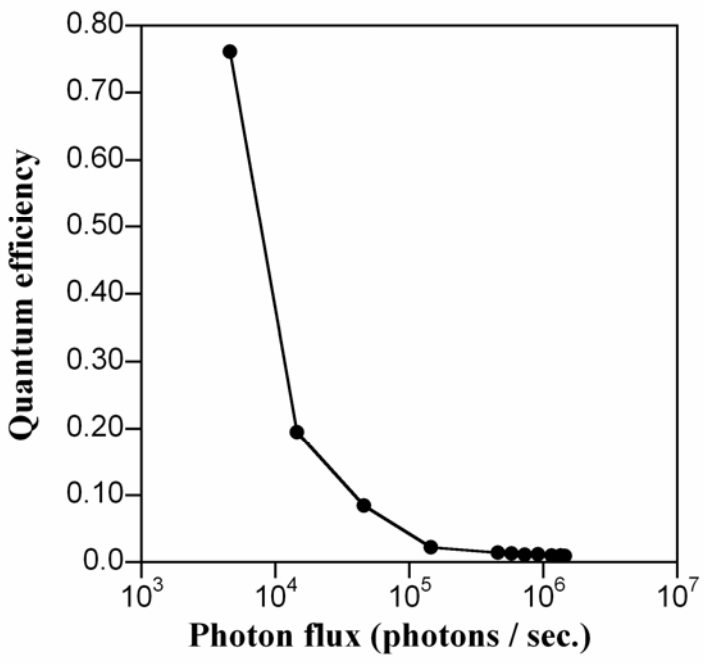

Figure 30. Inferred quantum efficiency as a function of photon flux.

6 Fluorescence Titration Experiment

Fura-2 [163] is a ratiometric fluorescent calcium ion indicator which operates by binding to free intracellular calcium. It is one of the most popular dyes used in calcium imaging applications and is extensively utilized for accurately quantifying intracellular calcium concentrations. Ratiometric measurements rely on a differential response of Fura-2 due to excitation at 340 or 380nm, where the ratio of emission intensities (at 510 nm) provides an estimate for the calcium concentration that is insensitive to changes in Fura-2 concentration, optical path distortions, and photobleaching. Fura-2 sensitivity of the SPAD detector was found by successively halving a stock concentration of fluorophore from 0.25 μM to 3.91 nM in HBSS (Hanks Balanced Salt Solution).

The count rate was first measured with HBSS only and then subsequently with Fura-2; the final count rate is the difference between the two. All measurements were made at 340 nm excitation using a commercial emission filter with a 420 nm longpass characteristic. The detection limit of the detector to Fura-2 was determined as the lowest concentration at which the count rate exceeded the background by at least one standard deviation, which occurred at 15.625 nM. In comparison with a low noise photodetector which had a detection limit of 39 nM, the SPAD detector is a factor of 2.3 better [31]. We are currently working on improving this detection limit by reducing the coupling efficiency of the excitation light with the chip.

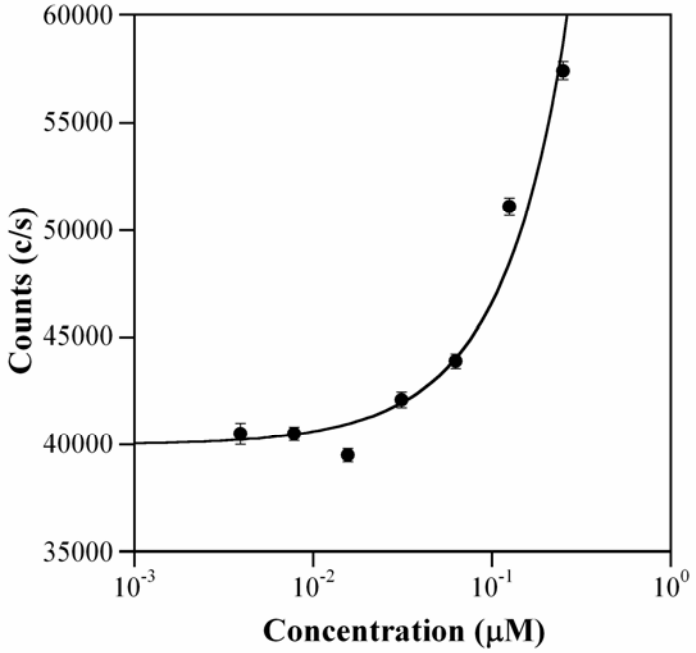

Figure 31. Detector response as a function of Fura-2 concentration. The experiment was conducted using a macroscopic commercial emission filter.

7 Conclusions

We demonstrated a single photon avalanche detector fabricated in a standard 0.5 μm nwell CMOS process. The detector exhibits a timing resolution of ~500 ns using offchip passive

quenching. This timing precision can be greatly improved using on-chip passive or active quenching. The detector was extensively characterized. The dark count was 16000 c/s at an excess bias voltage of 1.15 V at room temperature and increased steeply with excess bias voltage. The detector is sensitive to incident illumination over at least four orders of magnitude of intensity, and the quantum efficiency is highest at low intensities. The detector was used in a fluorescence experiment to demonstrate its potential for detecting low light levels. A 20 nM level of Fura-2 was reliably detected. This detection limit can be improved with better optical design of the setup, i.e. decoupling the excitation light with the detector.

Acknowledgement

We would like to thank our colleagues from the Integrated Biomorphic Information Systems laboratory for helpful discussions on the material presented in this paper. We particularly acknowledge Somashekar B. Prakash for his assistance with the data acquisition software. We also thank John Pyle of the Institute for Research in Electronics and Applied Physics for machining the fixture used in our fluorescence experiments. Finally, we thank Shyam Mehrotra for his help in selecting the high slew rate buffer. This work is supported by Quantum Molecular Pharmaceuticals, Inc., and the Maryland Industrial Partnerships (MIPS) program.

Chapter 5: Conclusions and Future Work

In Chapter 2, we reviewed a wide variety of spectral discrimination schemes. Our investigation revealed that neither one has been widely adopted. This is a consequence of the trade-offs between performance, complexity, and fabrication procedures. The microscale fluorometers that have been demonstrated to date work well with high brightness samples. However, the challenge for the next generation of devices is improving the sensitivity so that these systems can accomplish low-light tasks such as single-molecule detection. The set of performance metrics proposed will be useful for the rigorous design of sensors capable of reaching such detection levels.

In Chapter 3, we reported the design and testing of an organic optical filter and described a general methodology for evaluating the responsivity of solid state detectors used in microscale fluorometers. Using these methods, it was found that an active pixel sensor (APS), equipped with the filter, showed a maximum rejection of ~-20 dB at 370 nm. This rejection level is in contrast with spectrophotometric data which showed that the transmission of a 20 μm-thick spin-cast filter (on a glass slide) produced a maximum rejection of -30 dB (at 375 nm) for the particular concentration used (1 mM in the polymer precursor).

At this point, we can only formulate hypotheses explaining this discrepancy. It might be the case that there is a non-linear relationship between the photon flux incident on the photodiode and the detector response. This would account for the measurement showing that the detector is more responsive in the passband as opposed to what the filer transmission curve predicts. An experiment characterizing the response of the detector to specific photon fluxes would have to be

undertaken in order to investigate this statement. Alternatively, another factor that could explain this behavior is the uneven distribution of the absorbing molecules in the polymer matrix at large thicknesses. This could translate into a decrease in the filter's transmission efficiency thicknesses. In order to investigate this hypothesis, a set of experiments verifying the filter's transmission as a function of thickness (for a fixed loading concentration) should be carried out.

The fourth chapter of this thesis addressed another important aspect of micro-fluorometer design: low-noise solid state detectors. We demonstrated a single photon avalanche detector fabricated in a standard 0.5 μm nwell CMOS process. A 20 nM level of Fura-2 was reliably detected using this detector. This detection level was a factor 2 less than that of the filtered active pixel sensor discussed in Chapter 3. The single photon avalanche detector's detection limit can be further improved with better optical design of the setup, i.e., decoupling the excitation light with the detector, and by improving its dark count and timing resolution.

In summary, we have identified two fundamental aspects of micro-fluorometer design. They are: optical filter design and low-noise photon transduction. The performance of the fluorometers ultimately depends on the individual performance of each of these elements, but also on the methods with which they are integrated. The work discussed in this thesis will serve as a blueprint for the design and fabrication of future microscale fluorometers.

References

[1] J. R. Lakowicz *Principles of Fluorescence Spectroscopy*. New York: Plenum Publishing Corporation, 1983.

[2] E. Pham, J. Chiang, I. Li, W. Shum, and K. Truong, "A computational tool for designing FRET protein biosensors by rigid-body sampling of their conformational space," *Structure*, vol. 15, pp. 515-523, 2007.

[3] A. R. Brown and J. R. W. Govan, "Assessment of fluorescent in situ hybridization and PCR-based methods for rapid identification of Burkholderia cepacia complex organisms directly from sputum samples," *J. Clin. Microbiol.*, vol. 45, pp. 1920-1926, 2007.

[4] D. Psaltis, S. R. Quake, and C. H. Yang, "Developing optofluidic technology through the fusion of microfluidics and optics," *Nature*, vol. 442, pp. 381-386, 2006.

[5] J. R. Webster, M. A. Burns, D. T. Burke, and C. H. Mastrangelo, "Monolithic capillary electrophoresis device with integrated fluorescence detector," *Anal. Chem.*, vol. 73, pp. 1622-1626, 2001.

[6] M. Dandin, P. Abshire, and E. Smela, "Optical filtering technologies for integrated fluorescence sensors," *Lab Chip*, vol. 7, pp. 955 - 977, 2007.

[7] M. Dandin, N. M. Nelson, V. Saveliev, I. Weinberg, H. Ji, and P. Abshire, "Single Photon Avalanche Detectors in Standard CMOS," in *6th Annual IEEE Conference on Sensors*. Atlanta, Georgia, 2007.

[8] A. Manz, N. Graber, and H. M. Widmer, "Miniaturized total chemical analysis systems - a novel concept for chemical sensing," *Sens. Act. B*, vol. 1, pp. 244-248, 1990.

[9] N. Chiem and D. J. Harrison, "Microchip-based capillary electrophoresis for immunoassays: Analysis of monoclonal antibodies and theophylline," *Anal. Chem.*, vol. 69, pp. 373-378, 1997.

[10] Z. H. Liang, N. Chiem, G. Ocvirk, T. Tang, K. Fluri, and D. J. Harrison, "Microfabrication of a planar absorbance and fluorescence cell for integrated capillary electrophoresis devices," *Anal. Chem.*, vol. 68, pp. 1040-1046, 1996.

[11] N. V. Zaytseva, V. N. Goral, R. A. Montagna, and A. J. Baeumner, "Development of a microfluidic biosensor module for pathogen detection," *Lab Chip*, vol. 5, pp. 805-811, 2005.

[12] P. A. Auroux, D. Iossifidis, D. R. Reyes, and A. Manz, "Micro total analysis systems. 2. Analytical standard operations and applications," *Anal. Chem.*, vol. 74, pp. 2637-2652, 2002.

[13] P. A. Auroux, Y. Koc, A. deMello, A. Manz, and P. J. R. Day, "Miniaturised nucleic acid analysis," *Lab Chip*, vol. 4, pp. 534-546, 2004.

[14] T. Vilkner, D. Janasek, and A. Manz, "Micro total analysis systems. Recent developments," *Anal. Chem.*, vol. 76, pp. 3373-3385, 2004.

[15] C. H. Lin, G. B. Lee, L. M. Fu, and S. H. Chen, "Integrated optical-fiber capillary electrophoresis microchips with novel spin-on-glass surface modification," *Biosens. Bioelectron.*, vol. 20, pp. 83-90, 2004.

[16] A. Hanning, P. Lindberg, J. Westberg, and J. Roeraade, "Laser induced fluorescence detection by liquid core waveguiding applied to DNA sequencing by capillary electrophoresis," *Anal. Chem.*, vol. 72, pp. 3423-3430, 2000.

[17] S. L. Wang, X. J. Huang, Z. L. Fang, and P. K. Dasgupta, "A miniaturized liquid core waveguide-capillary electrophoresis system with flow injection sample introduction and fluorometric detection using light-emitting diodes," *Anal. Chem.*, vol. 73, pp. 4545-4549, 2001.

[18] C. H. Lin, G. B. Lee, S. H. Chen, and G. L. Chang, "Micro capillary electrophoresis chips integrated with buried SU-8/SOG optical waveguides for bio-analytical applications," *Sens. Act. A*, vol. 107, pp. 125-131, 2003.

[19] H. F. Li, Z. W. Cai, and J. M. Lin, "Separation of catecholamines by microchip electrophoresis with a simple integrated laser-induced fluorescence detector," *Anal. Chim. Acta*, vol. 565, pp. 183-189, 2006.

[20] A. Hanning, J. Westberg, and J. Roeraade, "A liquid core waveguide fluorescence detector for multicapillary electrophoresis applied to DNA sequencing in a 91-capillary array," *Electrophoresis*, vol. 21, pp. 3290-3304, 2000.

[21] X. L. Zhang, H. B. Yin, J. M. Cooper, and S. J. Haswell, "A microfluidic-based system for analysis of single cells based on Ca2+ flux," *Electrophoresis*, vol. 27, pp. 5093-5100, 2006.

[22] A. T. Woolley and R. A. Mathies, "Ultra-high-speed DNA sequencing using capillary electrophoresis chips," *Anal. Chem.*, vol. 67, pp. 3676-3680, 1995.

[23] P. C. Simpson, D. Roach, A. T. Woolley, T. Thorsen, R. Johnston, G. F. Sensabaugh, and R. A. Mathies, "High-throughput genetic analysis using microfabricated 96-sample capillary array electrophoresis microplates," *Proc. Natl. Acad. Sci. U. S. A.*, vol. 95, pp. 2256-2261, 1998.

[24] L. C. Waters, S. C. Jacobson, N. Kroutchinina, J. Khandurina, R. S. Foote, and J. M. Ramsey, "Microchip device for cell lysis, multiplex PCR amplification, and electrophoretic sizing," *Anal. Chem.*, vol. 70, pp. 158-162, 1998.

[25] E. T. Lagally, P. C. Simpson, and R. A. Mathies, "Monolithic integrated microfluidic DNA amplification and capillary electrophoresis analysis system," *Sens. Act. B*, vol. 63, pp. 138-146, 2000.

[26] A. Y. Fu, C. Spence, A. Scherer, F. H. Arnold, and S. R. Quake, "A microfabricated fluorescence-activated cell sorter," *Nat. Biotechnol.*, vol. 17, pp. 1109-1111, 1999.

[27] C. M. Chang, S. K. Hsiung, and G. B. Lee, "A micromachine-based flow cytometer chip integrated with micro-pumps/valves for multi-wavelength detection applications," *Mater. Sci. Forum*, vol. 505-507, pp. 637-642, 2006.

[28] Y. C. Tung, M. Zhang, C. T. Lin, K. Kurabayashi, and S. J. Skerlos, "PDMS-based opto-fluidic micro flow cytometer with two-color, multi-angle fluorescence detection capability using PIN photodiodes," *Sens. Act. B*, vol. 98, pp. 356-367, 2004.

[29] L. Cui, T. Zhang, and H. Morgan, "Optical particle detection integrated in a dielectrophoretic lab-on-a-chip," *J. Micromech. Microeng.*, vol. 12, pp. 7-12, 2002.

[30] J. Voldman, M. L. Gray, M. Toner, and M. A. Schmidt, "A microfabrication-based dynamic array cytometer," *Anal. Chem.*, vol. 74, pp. 3984-3990, 2002.

[31] D. Sander, M. Dandin, H. Ji, N. Nelson, and P. Abshire, "Low-noise CMOS fluorescence sensor," presented at IEEE Int. Symp. Circuits and Systems (ISCAS07), New Orleans, LA USA, 2007.

[32] E. J. Cho and F. V. Bright, "Optical sensor array and integrated light source," *Anal. Chem.*, vol. 73, pp. 3289-3293, 2001.

[33] P. Neuzil, J. Pipper, and T. M. Hsieh, "Disposable real-time microPCR device: lab-on-a-chip at a low cost," *Mol. Biosyst.*, vol. 2, pp. 292-298, 2006.

[34] P. Hua, J. P. Hole, J. S. Wilkinson, G. Proll, J. Tschmelak, G. Gauglitz, M. A. Jackson, R. Nudd, H. M. T. Griffith, R. A. Abuknesha, J. Kaiser, and P. Kraemmer, "Integrated optical fluorescence multisensor for water pollution," *Opt. Express*, vol. 13, pp. 1124-1130, 2005.

[35] S. H. Huang and F. G. Tseng, "Development of a monolithic total internal reflection-based biochip utilizing a microprism array for fluorescence sensing," *J. Micromech. Microeng.*, vol. 15, pp. 2235-2242, 2005.

[36] A. Cleary, S. Garcia-Blanco, A. Glidle, J. S. Aitchison, P. Laybourn, and J. M. Cooper, "An integrated fluorescence array as a platform for lab-on-a-chip technology using multimode interference splitters," *IEEE Sens. J.*, vol. 5, pp. 1315-1320, 2005.

[37] A. Zanzotto, P. Boccazzi, N. Gorret, T. K. Van Dyk, A. J. Sinskey, and K. F. Jensen, "In situ measurement of bioluminescence and fluorescence in an integrated microbioreactor," *Biotechnol. Bioeng.*, vol. 93, pp. 40-47, 2006.

[38] A. Zanzotto, N. Szita, P. Boccazzi, P. Lessard, A. J. Sinskey, and K. F. Jensen, "Membrane-aerated microbioreactor for high-throughput bioprocessing," *Biotechnol. Bioeng.*, vol. 87, pp. 243-254, 2004.

[39] L. J. Golonka, T. Zawada, J. Radojewski, H. Roguszczak, and M. Stefanow, "LTCC microfluidic system," *Int. J. Appl. Ceram. Technol.*, vol. 3, pp. 150-156, 2006.

[40] L. J. Golonka, H. Roguszczak, T. Zawada, J. Radojewski, I. Grabowska, M. Chudy, A. Dybko, Z. Brzozka, and D. Stadnik, "LTCC based microfluidic system with optical detection," *Sens. Act. B*, vol. 111, pp. 396-402, 2005.

[41] R. Irawan, C. M. Tay, S. C. Tjin, and C. Y. Fu, "Compact fluorescence detection using in-fiber microchannels - its potential for lab-on-a-chip applications," *Lab Chip*, vol. 6, pp. 1095-1098, 2006.

[42] D. Kelly, K. M. Grace, X. Song, B. I. Swanson, D. Frayer, S. B. Mendes, and N. Peyghambarian, "Integrated optical biosensor for detection of multivalent proteins," *Opt. Lett.*, vol. 24, pp. 1723-1725, 1999.

[43] A. Neubauer, D. Pum, U. B. Sleytr, I. Klimant, and O. S. Wolfbeis, "Fibre-optic glucose biosensor using enzyme membranes with 2-D crystalline structure," *Biosens. Bioelectron.*, vol. 11, pp. 317-325, 1996.

[44] J. A. Fruetel, R. F. Renzi, V. A. VanderNoot, J. Stamps, B. A. Horn, J. A. A. West, S. Ferko, R. Crocker, C. G. Bailey, D. Arnold, B. Wiedenman, W. Y. Choi, D. Yee, I. Shokair, E. Hasselbrink, P. Paul, D. Rakestraw, and D. Padgen, "Microchip separations of protein biotoxins using an integrated hand-held device," *Electrophoresis*, vol. 26, pp. 1144-1154, 2005.

[45] R. F. Renzi, J. Stamps, B. A. Horn, S. Ferko, V. A. VanderNoot, J. A. A. West, R. Crocker, B. Wiedenman, D. Yee, and J. A. Fruetel, "Hand-held microanalytical instrument for chip-based electrophoretic separations of proteins," *Anal. Chem.*, vol. 77, pp. 435-441, 2005.

[46] A. E. Bruno, S. Barnard, M. Rouilly, A. Waldner, J. Berger, and M. Ehrat, "All-solid state miniaturized fluorescence sensor array for the determination of critical gases and electrolytes in blood," *Anal. Chem.*, vol. 69, pp. 507-513, 1997.

[47] R. A. Yotter and D. M. Wilson, "A review of photodetectors for sensing light-emitting reporters in biological systems," *IEEE Sens. J.*, vol. 3, pp. 288-303, 2003.

[48] M. Wells, "Advances in optical detection strategies for reporter signal measurements," *Curr. Opin. Biotechnol.*, vol. 17, pp. 28-33, 2006.

[49] N. Vekshin, *Photonics of Biopolymers*. New York: Springer-Verlag, 2002.

[50] L. A. Herzenberg, D. Parks, B. Sahaf, O. Perez, and M. Roederer, "The history and future of the fluorescence activated cell sorter and flow cytometry: A view from Stanford," *Clin. Chem.*, vol. 48, pp. 1819-1827, 2002.

[51] S. Weiss, "Fluorescence spectroscopy of single biomolecules," *Science*, vol. 283, pp. 1676-1683, 1999.

[52] T. Hirschfeld, "Optical microscopic observation of single small molecules," *Appl. Optics*, vol. 15, pp. 2965-2966, 1976.

[53] R. A. Keller, W. P. Ambrose, P. M. Goodwin, J. H. Jett, J. C. Martin, and M. Wu, "Single molecule fluorescence analysis in solution," *Appl. Spectrosc.*, vol. 50, pp. A12-A32, 1996.

[54] J. A. Chediak, Z. S. Luo, J. G. Seo, N. Cheung, L. P. Lee, and T. D. Sands, "Heterogeneous integration of CdS filters with GaN LEDs for fluorescence detection microsystems," *Sens. Act. A*, vol. 111, pp. 1-7, 2004.

[55] H. A. Macleod, *Thin Film Optical Filters*. London: Institute of Physics Publishing, 2001.

[56] J. Karunamuni, K. E. Stitzer, D. Eastwood, K. J. Albert, D. R. Walt, S. B. Brown, and M. L. Myrick, "Interference filter refinement for artificial nose fluorescence sensing," *Opt. Eng.*, vol. 40, pp. 888-895, 2001.

[57] M. A. Burns, B. N. Johnson, S. N. Brahmasandra, K. Handique, J. R. Webster, M. Krishnan, T. S. Sammarco, P. M. Man, D. Jones, D. Heldsinger, C. H. Mastrangelo, and

D. T. Burke, "An integrated nanoliter DNA analysis device," *Science*, vol. 282, pp. 484-487, 1998.

[58] M. Adams, M. Enzelberger, S. Quake, and A. Scherer, "Microfluidic integration on detector arrays for absorption and fluorescence micro-spectrometers.," *Sens. Act. A*, vol. 104, pp. 25-31, 2002.

[59] Y.-H. Kim, K.-S. Shin, J.-Y. Kang, E.-G. Yang, K.-K. Paek, D.-S. Seo, and B.-K. Ju, "Poly(dimethylsiloxane)-based packaging technique for microchip fluorescence detection system applications," *J. Microelectromech. Syst.*, vol. 15, pp. 1152-1158, 2006.

[60] E. Thrush, O. Levi, W. Ha, K. Wang, S. J. Smith, and J. S. Harris Jr., "Integrated bio-fluorescence sensor," *J. Chromatogr. A*, vol. 1013, pp. 103-110, 2003.

[61] E. Thrush, O. Levi, K. Wang, J. J. S. Harris, and S. Smith, "Integrated semiconductor fluorescent detection system for biochip and biomedical applications," presented at 2nd Annual International IEEE-EMBS Special Topic Conference on Microtechnologies in Medicine & Biology, Madison, Wisconsin USA, 2002.

[62] V. Namasivayam, R. S. Lin, B. Johnson, S. Brahmasandra, Z. Razzacki, D. T. Burke, and M. A. Burns, "Advances in on-chip photodetection for applications in miniaturized genetic analysis systems," *J. Micromech. Microeng.*, vol. 14, pp. 81-90, 2004.

[63] H. Ji, D. Sander, A. Haas, and P. Abshire, "Contact imaging: simulation and experiment," *IEEE Trans. Circuits Syst. I-Regul. Pap.*, 2007.

[64] K. S. Shin, Y. H. Kim, K. K. Paek, J. H. Park, E. G. Yang, T. S. Kim, J. Y. Kang, and B. K. Ju, "Characterization of an integrated, fluorescence-detection hybrid device with photodiode and organic light-emitting diode," *IEEE Electron Device Letters*, vol. 27, pp. 746-748, 2006.

[65] E. Thrush, O. Levi, L. J. Cook, J. Deich, A. Kurtz, S. J. Smith, W. E. Moerner, and J. S. Harris Jr., "Monolithically integrated semiconductor fluorescence sensor for microfluidic applications," *Sens. Act. B*, vol. 105, pp. 393-399, 2005.

[66] E. Thrush, O. Levi, L. J. Cook, J. J. S. Harris, S. J. Smith, J. Deich, and W. E. Moerner, "Integrated semiconductor bio-fluorescence sensor integrated on micro-fluidic platform," presented at Conference on Lasers and Electro-Optics (CLEO) 2004, San Francisco, CA, 2004.

[67] E. Thrush, O. Levi, L. J. Cook, S. J. Smith, and J. J. S. Harris, "Greater than 10^6 optical isolation in integrated optoelectronic fluorescence sensor," presented at 26th Annual International Conference of the IEEE Engineering in Medicine and Biology Society (EMBS '04), San Francisco, CA, 2004.

[68] E. Thrush, O. Levi, W. Ha, G. Carey, L. J. Cook, J. Deich, S. J. Smith, W. E. Moerner, and J. J. S. Harris, "Integrated semiconductor vertical-cavity surface-emitting lasers and PIN photodetectors for biomedical fluorescence sensing," *IEEE J. Quantum Electron.*, vol. 40, pp. 491-8, 2004.

[69] E. P. Thrush, O. Levi, L. J. Cook, J. Deich, S. J. Smith, W. E. Moerner, and J. J. S. Harris, "Laser background characterization in a monolithically integrated bio-fluorescence sensor," presented at SPIE Conference on Advanced Biomedical and Clinical Diagnostic Systems II, San Jose, CA, 2004.

[70] H. D. Summers and P. A. Porta, "Resonant-cavity optoelectronic devices for fluorimetry," *IEEE J. Sel. Top. Quantum Electron.*, vol. 11, pp. 854-857, 2005.

[71] T. Kamei, B. M. Paegel, J. R. Scherer, A. M. Skelley, R. A. Street, and R. A. Mathies, "Integrated hydrogenated amorphous Si photodiode detector for microfluidic bioanalytical devices," *Anal. Chem.*, vol. 75, pp. 5300-5305, 2003.

[72] T. Kamei, B. M. Paegel, J. R. Scherer, A. M. Skelley, R. A. Street, and R. A. Mathies, "Fusion of a-Si : H sensor technology with microfluidic bioanalytical devices," *J. Non-Cryst. Solids*, vol. 338-40, pp. 715-719, 2004.

[73] G. Lammel and P. Renaud, "Free-standing, mobile 3D porous silicon microstructures," *Sens. Act. A*, vol. 85, pp. 356-360, 2000.

[74] G. Lammel, S. Schweizer, and P. Renaud, "Microspectrometer based on a tunable optical filter of porous silicon," *Sens. Act. A*, vol. 92, pp. 52-59, 2001.

[75] G. Lammel, S. Schweizer, S. Schiesser, and P. Renaud, "Tunable optical filter of porous silicon as key component for a MEMS spectrometer," *J. Microelectromech. Syst.*, vol. 11, pp. 815-828, 2002.

[76] E. Lorenzo, C. J. Oton, N. E. Capuj, M. Ghulinyan, D. Navarro-Urrios, Z. Gaburro, and L. Pavesi, "Porous silicon-based rugate filters," *Appl. Optics*, vol. 44, pp. 5415-5421, 2005.

[77] S. Langa, J. Carstensen, M. Christophersen, K. Steen, S. Frey, I. M. Tiginyanu, and H. Foll, "Uniform and nonuniform nucleation of pores during the anodization of Si, Ge, and III-V semiconductors," *J. Electrochem. Soc.*, vol. 152, pp. C525-C531, 2005.

[78] S. Lolkes, M. Christophersen, S. Langa, J. Carstensen, and H. Foll, "Selforganized formation of crystallographically oriented octahedral cavities during electrochemical pore etching," *Mater. Sci. Eng. B-Solid State Mater. Adv. Technol.*, vol. 101, pp. 159-163, 2003.

[79] H. Ouyang, M. Christophersen, R. Viard, B. L. Miller, and P. M. Fauchet, "Macroporous silicon microcavity for macromolecule detection," *Adv. Funct. Mater.*, vol. 15, 2005.

[80] H. Ouyang, M. Christophersen, and P. M. Fauchet, "Enhanced control of porous silicon morphology from macropore to mesopore formation," *Phys. Status Solidi A-Appl. Mat.*, vol. 202, pp. 1396-1401, 2005.

[81] J. R. Link and M. J. Sailor, "Smart dust: Self-assembling, self-orienting photonic crystals of porous Si," *Proc. Natl. Acad. Sci. U. S. A.*, vol. 100, pp. 10607-10610, 2003.

[82] M. Hochberg, T. Baehr-Jones, C. Walker, and A. Scherer, "Integrated plasmon and dielectric waveguides," *Opt. Express*, vol. 12, pp. 5481-5486, 2004.

[83] M. U. Gonzalez, J. C. Weeber, A. L. Baudrion, A. Dereux, A. L. Stepanov, J. R. Krenn, E. Devaux, and T. W. Ebbesen, "Design, near-field characterization, and modeling of 45 circle surface-plasmon Bragg mirrors," *Phys. Rev. B*, vol. 73, 2006.

[84] J. C. Weeber, Y. Lacroute, A. Dereux, E. Devaux, T. Ebbesen, C. Girard, M. U. Gonzalez, and A. L. Baudrion, "Near-field characterization of Bragg mirrors engraved in surface plasmon waveguides," *Phys. Rev. B*, vol. 70, 2004.

[85] J. R. Krenn, H. Ditlbacher, G. Schider, A. Hohenau, A. Leitner, and F. R. Aussenegg, "Surface plasmon micro- and nano-optics," *J. Microsc.-Oxf.*, vol. 209, pp. 167-172, 2003.

[86] A. Boltasseva, S. I. Bozhevolnyi, T. Nikolajsen, and K. Leosson, "Compact Bragg gratings for long-range surface plasmon polaritons," *J. Lightwave Technol.*, vol. 24, pp. 912-918, 2006.

[87] S. Jette-Charbonneau, R. Charbonneau, N. Lahoud, G. Mattiussi, and P. Berini, "Demonstration of Bragg gratings based on long-ranging surface plasmon polariton waveguides," *Opt. Express*, vol. 13, pp. 4674-4682, 2005.

[88] S. Jette-Charbonneau, R. Charbonneau, N. Lahoud, G. A. Mattiussi, and P. Berini, "Bragg gratings based on long-range surface plasmon-polariton waveguides: Comparison of theory and experiment," *IEEE J. Quantum Electron.*, vol. 41, pp. 1480-1491, 2005.

[89] Z. H. Han, E. Forsberg, and S. L. He, "Surface plasmon Bragg gratings formed in metal-insulator-metal waveguides," *IEEE Photonics Technol. Lett.*, vol. 19, pp. 91-93, 2007.

[90] A. Hosseini and Y. Massoud, "A low-loss metal-insulator-metal plasmonic bragg reflector," *Opt. Express*, vol. 14, pp. 11318-11323, 2006.

[91] A. Hosseini and Y. Massoud, "Subwavelength plasmonic Bragg reflector structures for on-chip optoelectronic applications," presented at IEEE Int. Symp. Circuits and Systems (ISCAS07), New Orleans, LA, 2007.

[92] J. A. Dionne, L. A. Sweatlock, H. A. Atwater, and A. Polman, "Planar metal plasmon waveguides: frequency-dependent dispersion, propagation, localization, and loss beyond the free electron model," *Phys. Rev. B*, vol. 72, 2005.

[93] J. A. Dionne, L. A. Sweatlock, H. A. Atwater, and A. Polman, "Plasmon slot waveguides: Towards chip-scale propagation with subwavelength-scale localization," *Phys. Rev. B*, vol. 73, 2006.

[94] W. L. Barnes, A. Dereux, and T. W. Ebbesen, "Surface plasmon subwavelength optics," *Nature*, vol. 424, pp. 824-830, 2003.

[95] E. Ozbay, "Plasmonics: Merging photonics and electronics at nanoscale dimensions," *Science*, vol. 311, pp. 189-193, 2006.

[96] R. R. Chance, A. Prock, and R. Silbey, "Comments on Classical Theory of Energy-Transfer," *J. Chem. Phys.*, vol. 62, pp. 2245-2253, 1975.

[97] H. Ditlbacher, J. R. Krenn, N. Felidj, B. Lamprecht, G. Schider, M. Salerno, A. Leitner, and F. R. Aussenegg, "Fluorescence imaging of surface plasmon fields," *Appl. Phys. Lett.*, vol. 80, pp. 404-406, 2002.

[98] S. C. Kitson, W. L. Barnes, J. R. Sambles, and N. P. K. Cotter, "Excitation of molecular fluorescence via surface plasmon polaritons," *J. Mod. Opt.*, vol. 43, pp. 573-582, 1996.

[99] M. Kreiter, T. Neumann, S. Mittler, N. Knoll, and J. R. Sambles, "Fluorescent dyes as a probe for the localized field of coupled surface plasmon-related resonances," *Phys. Rev. B*, vol. 64, 2001.

[100] O. Stranik, H. M. McEvoy, C. McDonagh, and B. D. MacCraith, "Plasmonic enhancement of fluorescence for sensor applications," *Sens. Act. B*, vol. 107, pp. 148-153, 2005.

[101] M. Tuma and R. Gruhlke, "Integrated Fluorescence." US, 1998.

[102] G. C. Giakos, K. Meehan, and M. Tuma, "Exploitation of enhanced fluorescence via cross-coupling principles toward the design of an optical integrated thin-film sensor for nanotechnology and biomedical applications," *IEEE Trans. Instrum. Meas.*, vol. 51, pp. 970-975, 2002.

[103] R. Muller, T. Kamins, and M. Chan, *Device Electronics for Integrated Circuits*, 3rd ed: John Wiley & Sons, 2003.

[104] S. Ninomiya and S. Adachi, "Optical properties of wurtzite CdS," *J. Appl. Phys.*, vol. 78, pp. 1183-1190, 1995.

[105] O. Yadid-Pecht and R. Etienne-Cummings, "CMOS Imagers: From Phototransduction to Image Processing." Norwell, MA: Kluwer Academic Publishers, 2004.

[106] D. R. Lide, "CRC Handbook of Physics and Chemistry," 87 ed. Boca Raton: CRC Press, 2006.

[107] J. Rabek, *Photostabilization of Polymers*, 1st ed. Stockholm: Elsevier Applied Science, 1990.

[108] G. Kovacs, *Micromachined Transducers Sourcebook*: McGraw-Hill, 1998.

[109] A. H. Mahan, R. Biswas, L. M. Gedvilas, D. L. Williamson, and B. C. Pan, "On the influence of short and medium range order on the material band gap in hydrogenated amorphous silicon," *J. Appl. Phys.*, vol. 96, pp. 3818-3826, 2004.

[110] H. Ji, M. Dandin, E. Smela, and P. Abshire, "Integrated Fluorescence Sensing for Lab-on-a-chip Devices," presented at IEEE/NLM Life Science Systems and Applications Workshop Bethesda, Maryland, 2006.

[111] K. Long, F. Pschenitzka, M. H. Lu, and J. C. Sturm, "Full-color OLEDs integrated by dry dye printing," *IEEE Trans. Electron Devices*, vol. 53, pp. 2250-2258, 2006.

[112] T. Graves-Abe, F. Pschenitzka, H. Z. Jin, B. Bollman, J. C. Sturm, and R. A. Register, "Solvent-enhanced dye diffusion in polymer thin films for polymer light-emitting diode application," *J. Appl. Phys.*, vol. 96, pp. 7154-7163, 2004.

[113] D. J. Guerrero, B. DiMenna, T. Flaim, R. Mercado, and S. Sun, "Dyed red, green, and blue photoresist for manufacture of high resolution color filter arrays for image sensors," presented at Sensors and Camera Systems for Scientific, Industrial and Digital Photography Applications IV, 2003.

[114] M. Muasher and M. Sain, "The efficacy of photo stabilizers on the color change of wood filled plastic composites," *Polym. Degrad. Stabil.*, vol. 91, pp. 1156-1165, 2006.

[115] G. A. Peyman, H. Sloan, and J. Lim, "Ultraviolet light absorbing pseudophakos," *J. Am. Intraocul. Implant. Soc.*, vol. 8, pp. 357-360, 1982.

[116] V. P. Iordanov, J. Bastemeijer, R. Ishihara, P. M. Sarro, A. Bossche, and M. J. Vellekoop, "Filter-protected photodiodes for high-throughput enzymatic analysis," *IEEE Sens. J.*, vol. 4, pp. 584-588, 2004.

[117] M. L. Chabinyc, D. T. Chiu, J. C. McDonald, A. D. Stroock, J. F. Christian, A. M. Karger, and G. M. Whitesides, "An integrated fluorescence detection system in poly(dimethylsiloxane) for microfluidic applications," *Anal. Chem.*, vol. 73, pp. 4491-4498, 2001.

[118] J. Kruger, K. Singh, A. O'Neill, C. Jackson, A. Morrison, and P. O'Brien, "Development of a microfluidic device for fluorescence activated cell sorting," *J. Micromech. Microeng.*, vol. 12, pp. 486-494, 2002.

[119] O. Hofmann, X. H. Wang, A. Cornwell, B. Stephen, A. Raja, D. Bradley, A. deMello, and J. deMello, "Monolithically integrated dye-doped PDMS long-pass filters for disposable on-chip fluorescence detection," *Lab Chip*, vol. 6, pp. 981-987, 2006.

[120] O. J. A. Schueller, D. C. Duffy, J. A. Rogers, S. T. Brittain, and G. M. Whitesides, "Reconfigurable diffraction gratings based on elastomeric microfluidic devices," *Sens. Act. A*, vol. 78, pp. 149-159, 1999.

[121] C. C. Chen, D. Hirdes, and A. Folch, "Gray-scale photolithography using microfluidic photomasks," *Proc. Natl. Acad. Sci. U. S. A.*, vol. 100, pp. 1499-1504, 2003.

[122] R. B. Merrill, "Color separation in an active pixel cell imaging array using a triple-well structure." USA: Foveon, Inc., 1999.

[123] R. Lyon and P. Hubel, "Eyeing the camera: into the next century," presented at Tenth Color Imaging Conference: Color Science and Engineering Systems, Technologies, Applications, Scottsdale, Arizona, 2002.

[124] D. Starikov, F. Benkabou, N. Medelci, and A. Bensaoula, "Integrated multi-wavelength fluorescence sensors," presented at Sensors for Industry Conference, 2nd ISA/IEEE, 2002.

[125] Y. Maruyama, K. Sawada, H. Takao, and M. Ishida, "The fabrication of filter-less fluorescence detection sensor array using CMOS image sensor technique," *Sens. Act. A*, vol. 128, pp. 66-70, 2006.

[126] Y. Maruyama, K. Sawada, H. Takao, and M. Ishida, "A novel filterless fluorescence detection sensor for DNA analysis," *IEEE Trans. Electron Devices*, vol. 53, pp. 553-558, 2006.

[127] R. F. Wolffenbuttel, "State-of-the-art in integrated optical microspectrometers," *IEEE Trans. Instrum. Meas.*, vol. 53, pp. 197-202, 2004.

[128] R. F. Wolffenbuttel, "MEMS-based optical mini- and microspectrometers for the visible and infrared spectral range," *J. Micromech. Microeng.*, vol. 15, pp. S145-S152, 2005.

[129] O. Hofmann, X. H. Wang, J. C. deMello, D. D. C. Bradley, and A. J. deMello, "Towards microalbuminuria determination on a disposable diagnostic microchip with integrated fluorescence detection based on thin-film organic light emitting diodes," *Lab Chip*, vol. 5, pp. 863-868, 2005.

[130] V. Lien, K. Zhao, Y. Berdichevsky, and Y. H. Lo, "High-sensitivity cytometric detection using fluidic-photonic integrated circuits with array waveguides," *IEEE J. Sel. Top. Quantum Electron.*, vol. 11, pp. 827-834, 2005.

[131] G. M. Yee, N. I. Maluf, P. A. Hing, M. Albin, and G. T. A. Kovacs, "Miniature spectrometers for biochemical analysis," *Sens. Act. A*, vol. 58, pp. 61-66, 1997.

[132] M. A. Powers, S. T. Koev, A. Schleunitz, H. Yi, V. Hodzic, W. E. Bentley, G. F. Payne, G. W. Rubloff, and R. Ghodssi, "A fabrication platform for electrically mediated optically active biofunctionalized sites in BioMEMS," *Lab Chip*, vol. 5, pp. 583-586, 2005.

[133] J. M. Ruano, A. Glidle, A. Cleary, A. Walmsley, J. S. Aitchison, and J. M. Cooper, "Design and fabrication of a silica on silicon integrated optical biochip as a fluorescence microarray platform," *Biosens. Bioelectron.*, vol. 18, pp. 175-184, 2003.

[134] P. N. Zeller, G. Voirin, and R. E. Kunz, "Single-pad scheme for integrated optical fluorescence sensing," *Biosens. Bioelectron.*, vol. 15, pp. 591-595, 2000.

[135] K. Miyaki, Y. L. Guo, T. Shimosaka, T. Nakagama, H. Nakajima, and K. Uchiyama, "Fabrication of an integrated PDMS microchip incorporating an LED-induced fluorescence device," *Anal. Bioanal. Chem.*, vol. 382, pp. 810-816, 2005.

[136] J. C. Roulet, R. Volkel, H. P. Herzig, E. Verpoorte, N. F. de Rooij, and R. Dandliker, "Fabrication of multilayer systems combining microfluidic and microoptical elements for fluorescence detection," *J. Microelectromech. Syst.*, vol. 10, pp. 482-491, 2001.

[137] J. C. Roulet, R. Volkel, H. P. Herzig, E. Verpoorte, N. F. de Rooij, and R. Dandliker, "Microlens systems for fluorescence detection in chemical microsystems," *Opt. Eng.*, vol. 40, pp. 814-821, 2001.

[138] J. C. Roulet, R. Volkel, H. P. Herzig, E. Verpoorte, N. F. de Rooij, and R. Dandliker, "Performance of an integrated microoptical system for fluorescence detection in microfluidic systems," *Anal. Chem.*, vol. 74, pp. 3400-3407, 2002.

[139] M. Zourob, S. Mohr, B. J. T. Brown, P. R. Fielden, M. McDonnell, and N. J. Goddard, "The development of a metal clad leaky waveguide sensor for the detection of particles," *Sens. Act. B*, vol. 90, pp. 296-307, 2003.

[140] M. Zourob, S. Mohr, B. J. T. Brown, P. R. Fielden, M. B. McDonnell, and N. J. Goddard, "An integrated metal clad leaky waveguide sensor for detection of bacteria," *Anal. Chem.*, vol. 77, pp. 232-242, 2005.

[141] M. Zourob, S. Mohr, B. J. T. Brown, P. R. Fielden, M. B. McDonnell, and N. J. Goddard, "An integrated optical leaky waveguide sensor with electrically induced concentration system for the detection of bacteria," *Lab Chip*, vol. 5, pp. 1360-1365, 2005.

[142] M. Zourob, S. Mohr, B. J. T. Brown, P. R. Fielden, M. B. McDonnell, and N. J. Goddard, "Bacteria detection using disposable optical leaky waveguide sensors," *Biosens. Bioelectron.*, vol. 21, pp. 293-302, 2005.

[143] M. Zourob, S. Mohr, P. R. Fielden, and N. J. Goddard, "Small-volume refractive index and fluorescence sensor for micro total analytical system (mu-TAS) applications," *Sens. Act. B*, vol. 94, pp. 304-312, 2003.

[144] M. Zourob, S. Mohr, P. R. Fielden, and N. J. Goddard, "An integrated disposable dye clad leaky waveguide sensor for μTAS applications," *Lab Chip*, vol. 5, pp. 772-777, 2005.

[145] M. Zourob, A. Simonian, J. Wild, S. Mohr, X. D. Fan, I. Abdulhalim, and N. J. Goddard, "Optical leaky waveguide biosensors for the detection of organophosphorus pesticides," *Analyst*, vol. 132, pp. 114-120, 2007.

[146] J. Seo and P. L. Lee, "Fluorescence amplification by self-aligned integrated microfluidic optical systems," presented at Transducers, Boston, USA, 2003.

[147] T. Daud, J. R. Janesick, K. Evans, and T. Elliott, "Charge-coupled-device response to electron beam energies of less than 1 keV up to 20 keV," *Opt. Eng.*, vol. 26, pp. 686-91, 1987.

[148] B. Fowler, A. E. Gamal, D. Yang, and H. Tian, "A method for estimating quantum efficiency for CMOS image sensors," presented at SPIE Conference on Solid State Sensor Arrays: Development and Applications II. , USA, San Jose, CA, 1998.

[149] A. v. d. Ziel, *Noise in Solid State Devices and Circuits*. New York, NY: John Wiley & Sons, Inc., 1986.

[150] C. D. Motchenbacher and J. A. Connelly, *Low Noise Electronic System Design*. New York, NY: John Wiley & Sons, Inc., 1993.

[151] B. E. A. Saleh and M. C. Teich, *Fundamentals of Photonics*. New York , NY: John Wiley & Sons, Inc., 1991.

[152] A. Schwartz, L. Wang, E. Early, A. Gaigalas, Y.-z. Zhang, G. E. Marti, and R. F. Vogt, "Quantitating fluorescence intensity from fluorophore: The definition of MESF assignment," *J. Res. Natl. Inst. Stand. Technol.*, vol. 107, pp. 83-91, 2002.

[153] A. K. Gaigalas, L. Wang, A. Schwartz, G. E. Marti, and J. R. F. Vogt, "Quantitating fluorescence intensity from fluorophore: assignment of MESF values," *J. Res. Natl. Inst. Stand. Technol.*, vol. 110, pp. 101-14, 2005.

[154] R. E. Lee, C. Neri, V. Malatesta, R. M. Riva, and M. Angaroni, "A new family of benzotriazoles: how to modulate properties within the same technology," in *Specialty Polymer Additives*, S. Al-Malaika, A. Golovoy, and C. A. Wilkie, Eds. Cornwall: Blackwell Science, 2001.

[155] C. Decker, "Photostabilization of UV-cured coatings and thermosets," in *Specialty Polymer Additives*, S. Al-Malaika, A. Golovoy, and C. A. Wilkie, Eds. Cornwall: Blackwell Science, 2001.

[156] N. Nelson, S. Prakaksh, D. Sander, M. Dandin, A. Sarje, H. Ji, and P. Abshire, "A Handheld Fluorometer for UV Excitable Fluorescence Assays," in *IEEE Biomedical Circuits and Systems Conference*. Montreal, Canada, 2007.

[157] C. Niclass, A. Rochas, P. A. Besse, and E. Charbon, "Toward a 3-D camera based on single photon avalanche diodes," *IEEE J. Sel. Top. Quantum Electron.*, vol. 10, pp. 796-802, 2004.

[158] C. Niclass, A. Rochas, P. A. Besse, and E. Charbon, "Design and characterization of a CMOS 3-D image sensor based on single photon avlanche diodes," *IEEE J. Solid-State Circuit*, vol. 40, 2005.

[159] C. Niclass, A. Rochas, P. A. Besse, R. Popovic, and E. Charbon, "A 4 μs time imager based on CMOS single photon avalanche diode technology," *Sens. Act. A.*, vol. 130, pp. 273-281, 2006.

[160] A. Rochas, A. Pauchard, P. A. Besse, D. Pantic, Z. Prijic, and R. Popovic, "Low-noise silicon avalanche photodiodes fabricated in conventional CMOS technologies," *IEEE Trans. Electron Devices*, vol. 49, pp. 387-394, 2002.

[161] A. Rochas, M. Gosch, A. Serov, P. A. Besse, R. Popovic, T. Lasser, and R. Rigler, "First fully integrated 2-D array of single photon detectors in standard CMOS technology," *IEEE Photonics Technol. Lett.*, vol. 15, pp. 963-965, 2003.

[162] K. H. Wong, P. Cheng, S. Adler, V. Saveliev, S. K. Mun, and I. N. Weinberg, "PET-glove: a new technology for portable molecular imaging," in *SPIE*. San Diego, California, 2007.

[163] Invitrogen Corporation, "Fura and Indo ratiometric Calcium Indicators," 2006.